High-entropy ceramics

Corey Oses[1,2], *Cormac Toher*[1,2] *and Stefano Curtarolo*[1,2]✉

Abstract | Disordered multicomponent systems, occupying the mostly uncharted centres of phase diagrams, were proposed in 2004 as innovative materials with promising applications. The idea was to maximize the configurational entropy to stabilize (near) equimolar mixtures and achieve more robust systems, which became known as high-entropy materials. Initial research focused mainly on metal alloys and nitride films. In 2015, entropy stabilization was demonstrated in a mixture of oxides. Other high-entropy disordered ceramics rapidly followed, stimulating the addition of more components to obtain materials expressing a blend of properties, often highly enhanced. The systems were soon proven to be useful in wide-ranging technologies, including thermal barrier coatings, thermoelectrics, catalysts, batteries and wear-resistant and corrosion-resistant coatings. In this Review, we discuss the current state of the disordered ceramics field by examining the applications and the high-entropy features fuelling them, covering both theoretical predictions and experimental results. The influence of entropy is unavoidable and can no longer be ignored. In the space of ceramics, it leads to new materials that, both as bulk and thin films, will play important roles in technology in the decades to come.

From the early tools of primitive humans to the industrial revolution, development of railroads and space exploration, progress has hinged on the performance of available materials. Channelling properties through mixtures — alloying — is an age-old method to improve materials. Intuition dictates that a mixture should yield an average of its components' properties, but sometimes enhanced or otherwise entirely new features can arise. In highly disordered, multicomponent systems[1–7], high entropy produces attractive qualities, including a preference for single-phase solid solutions with simple crystal structures, sluggish kinetics, lattice distortions and a collection of properties surpassing those of the constituent materials[8]. The world of high-entropy materials is versatile: by adding species, unexpected properties emerge, which can then be fine-tuned by tailoring concentrations. The huge amount of possibilities for discovering ad hoc disordered materials can be addressed with efficient high-throughput approaches[9,10] and accelerated artificial intelligence methods[11,12]. Although disordered systems have been known for decades, an unambiguous demonstration of entropy stabilization caught the attention of the community in 2015 (REF.[13]). Not only did this present the first confirmed case of an entropy-driven transition to a homogeneous, single-phase system but it also introduced a new family of materials: entropy-stabilized oxides. High-entropy materials have since expanded to include borides[14], carbides[15–17], nitrides[18], sulfides[19] and silicides[20,21], which have remarkable properties leading to applications in thermal and environmental protection, thermoelectricity, water splitting, catalysis and energy storage.

Despite ongoing debate regarding the relevance of high-entropy effects in metal alloys[22–26], they appear to be important in high-entropy ceramics (FIG. 1), which remain single phase under extreme temperatures[27–32], pressures[30] and chemical environments[28,29,31,33–38], demonstrating stability and resilience across applications (TABLE 1). Synthesized at elevated temperatures, the structures can be quenched and remain stable at room temperature, a bonus of slow kinetics. Corrosion resistance appears in various systems. This might arise from sluggish diffusion, from amorphous or nanocrystalline microstructure, and from the incorporation of elements such as Al and Si (forming passivation layers preventing oxygen penetration)[39,40]. Low, amorphous-like thermal conductivity is associated with lattice distortions; coupled with high stiffness, it promotes thermal and environmental barrier protection[41]. Mechanical properties can be enhanced by lattice distortions arising from many differently sized elements (solid-solution strengthening)[3,42], by a nanograin microstructure impeding the motion of dislocations (Hall–Petch strengthening)[43] and by changes in and/or elimination of lattice slip systems[16]. The inhibition of grain coarsening, even at high temperatures, has been attributed to lattice distortions increasing the crystalline energy, thus reducing the free energy gained by shrinking the grain surface area[44]. The elastic modulus and hardness of high-entropy carbides have also been observed to depend on the valence electron concentration[45]. The mechanisms underlying these properties, often difficult to establish, become research opportunities for computational modelling.

[1]*Department of Mechanical Engineering and Materials Science, Duke University, Durham, NC, USA.*

[2]*Center for Autonomous Materials Design, Duke University, Durham, NC, USA.*

✉*e-mail: stefano@duke.edu*

https://doi.org/10.1038/s41578-019-0170-8

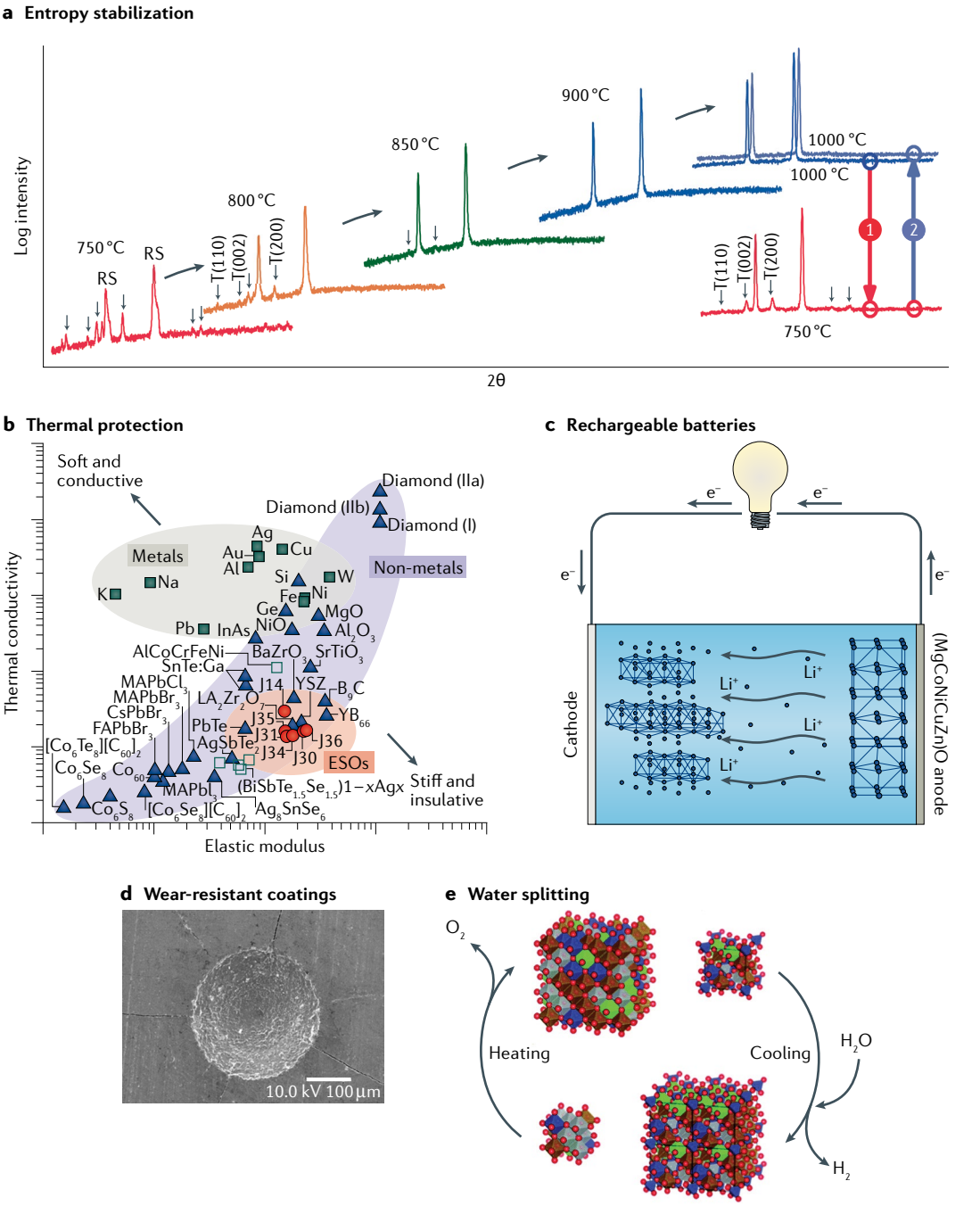

Fig. 1 | **Applications of high-entropy ceramics.** X-ray diffraction patterns of an equimolar mixture of MgO, NiO, ZnO, CuO and CoO at different temperatures. Peaks associated with secondary phases (indicated by the arrows), such as tenorite CuO (labelled with T), fade with increasing temperature, indicating the onset of entropy stabilization yielding a single-phase, rock-salt system. Peaks corresponding to rock-salt phases are indicated with RS. The transition between single-phase and multiphase systems is reversible and occurs between 750 and 1000 °C, as shown by bringing a sample equilibrated at 1000 °C down to 750 °C (arrow 1) and then back to 1000 °C (arrow 2) (part **a**). High-entropy effects can be employed for several applications, including: thermal protection, thanks to their combination of stiffness and low thermal conductivity, as seen in the thermal conductivity versus elastic modulus plot in which filled squares indicate metals, open squares high-entropy alloys, triangles non-metals and circles entropy-stabilized oxides (ESOs: J14 (MgCoNiCuZn)O, J30 (MgCoNiCuZnSc)O, J31 (MgCoNiCuZnSb)O, J34 (MgCoNiCuZnSn)O, J35 (MgCoNiCuZnCr)O, J36 (MgCoNiCuZnGe)O) (part **b**); rechargeable batteries, owing to their robust lithium-ion cycling stability induced by entropy stabilization (part **c**); Rockwell-C hardness tests for (AlCrNbSiTiV)N film coatings showing smooth indentations with minimal cracking, indicating good adhesion to the surface and high toughness, which are important for wear resistance (part **d**); and water splitting, as in the two-step reaction shown in the schematic, in which a metal oxide becomes reduced at high temperature, releasing O_2, and is then cooled and oxidized by water to produce H_2. A reversible phase transition occurs during cycling, rock-salt (reduced) to spinel (oxidized) (part **e**). Part **a** adapted from REF.[13], CC-BY-4.0 (https://creativecommons.org/licenses/by/4.0/). Part **b** adapted with permission from REF.[41], Wiley-VCH. Part **c** adapted from REF.[117], Elsevier. Part **d** reproduced with permission from REF.[170], Elsevier. Part **e** adapted with permission from REF.[119], Royal Society of Chemistry.

Table 1 | **High-entropy ceramics for bulk materials applications**

Year	Material	Description	Refs
Bulk structural materials			
2015	(MgCoNiCuZn)O	fcc lattice, entropy-stabilized, antiferromagnetic, T_N = 106–140 K	13,76,85,86
2016	Refractory borides	Hexagonal lattice, H = 17–27 GPa, fracture toughness = 3.64–4.47 MPa $m^{1/2}$	14,113
2017	(Ce{*RE*})O_2	Three to six cations: fluorite (CaF_2-type) structure; seven cations: cubic structure (space group $Ia\bar{3}$ #206); E_{gap} = 1.95–2.14 eV direct and 1.42–1.64 eV indirect	87,88
2018	Perovskite oxides	Two cation sublattices; ({Sr,Ba})({*M*})O_3: cubic structure (space group $Pm\bar{3}m$ #221); ({*RE*})({*TM*})O_3: orthorhombic structure (space group *Pbnm* #62), complex antiferromagnetic-dominated magnetic state	27,91,92,96
2018	$(CoCrFeMnNi)_3O_4$	Spinel structure, retains ferrimagnetic behaviour of other MFe_2O_4 spinels	97,98
2018	(HfNbTaTiZr)C	fcc lattice, H = 15–40.6 GPa, E = 443–552 GPa, κ = 5.42–6.45 W m^{-1} K^{-1}, oxidation resistant to 800 °C (versus 200 °C for binary carbides)	15,17,35,45,160
2018	(MoNbTaVW)C	fcc lattice, highest EFA despite two non-fcc precursors, H = 27 GPa, E = 533 GPa	15,45
2018	(HfTaTiWZr)C	fcc lattice, H = 33 GPa, E = 473 GPa	15,45
2018	(HfNbTaZr)C	fcc lattice, H = 36.1 GPa, E = 598 GPa	16
2019	$(GdTbDyHoEr)_2O_3$	Bixbyite structure, non-reversible transformation to single phase, paramagnet	102
2019	$(CoCrFeMnZn)_3O_4$ and $(CoCrFeNiZn)_3O_4$	Spinel structure, ferromagnets	99
2019	(NbTaZr)C	fcc lattice, flexural strength = 366–496 MPa, toughness = 2.9 MPa $m^{1/2}$, E = 563 GPa	161
2019	(MoNbTaTiVW)C(N)	fcc lattice, H = 28 GPa, E = 554.9 GPa, fracture toughness = 8.4 MPa $m^{1/2}$	162
2019	(HfMoTaTi)(BC)	Three phases (two fcc, one hexagonal), H = 27.4 GPa, E = 505.8 GPa	163
2019	(HfMoTaTi)(BC)–SiC	Composite (hcp high-entropy phase and SiC compound), H = 35.4 GPa, E = 472.4 GPa	164
2019	(MoNbTaTiW)Si_2	Hexagonal lattice, H = 11.6 GPa, κ = 6.9 W m^{-1} K^{-1}	20
2019	(MoNbTiWZr)Si_2	Hexagonal lattice, H = 12.09 GPa, E = 352 GPa	21
Energy-storage materials			
2016	(MgCoNiCuZn)O and derivatives	fcc lattice, anode material, specific capacity (I = 0.1 A g^{-1}, 300 cycles) = 920 mAh g^{-1}, approximately full capacity retention after 300 cycles; with Li_xF_x: colossal $\epsilon_r \approx 2 \times 10^5$, superionic Li conductivity >10^{-3} S cm^{-1}; with Li_xF_x: cathode material, working potential (versus Li^+/Li) = 3.4 V, specific capacity (I = 20 mA g^{-1}, 300 cycles) ≈ 120 mAh g^{-1}, 90% coulombic efficiencies after 300 cycles	38,63,64,116
2018	(CrMoNbVZr)N	fcc lattice, C = 78 F g^{-1} at 100 mV s^{-1} scan rate	18
Thermochemical water-splitting materials			
2018	$(MgCoNiFe)O_{1.2}$	Mixed-phase (rock-salt and spinel), H_2 yields (1300 °C) = 10.1 ± 0.5 ml-H_2 g^{-1}, H_2 yields (1100 °C) = 1.4 ± 0.5 ml-H_2 g^{-1}	119
Catalysts			
2018	Pt/Ru-loaded (MgCoNiCuZn)O	CO oxidation: completely converted at 155 °C, no catalytic activity reduction after >40 h at 135 °C; CO_2 hydrogenation at 500 °C: CO yields and CO_2 conversions >45%, CO selectivities >95%	74,77
Materials for thermal and environmental protection			
2018	(MgCoNiCuZn)O	fcc lattice, E = 108–152 GPa, bulk modulus = 187.7 ± 3.5 GPa, bending strength = 323 ± 19 MPa, κ = 2.95 ± 0.25 W m^{-1} K^{-1}, volumetric heat capacity = 3.01 ± 0.49 MJ m^{-3} K^{-1}, thermally stable ~450 °C and mechanically stable to ~50 GPa	30,41,82
2018	(HfZrCe)({*M*})$O_{2-\delta}$	Fluorite (CaF_2-type) structure, H = 12.3–13.6 GPa, κ = 1.1–1.81 W m^{-1} K^{-1}	89,90
2019	$(YbYLuScGd)_2Si_2O_7$	Monoclinic structure, stable up to 1300 °C, α = 3.7–5.7 × 10^{-6} K^{-1}, coated on C_f/SiC enduring a 50% H_2O–50% O_2 environment at 1250 °C for 300 h: residual flexural strength = 352 ± 26 MPa, strength retention = 86%	28
2019	$(YHoErYb)_2SiO_5$	Monoclinic structure, E(300–1600 °C) = 150–165 GPa, κ(300–1300 °C) ≈ 2 W m^{-1} K^{-1}, α(650–1450 °C) = 5.5–6.5 × 10^{-6} K^{-1}	29
2019	$(TiZrHf)P_2O_7$	Metal pyrophosphate structure, κ(300 K) = 0.78 W m^{-1} K^{-1}, higher thermal stability than single-component phases (>1550 °C)	31
2019	Pyrochlore oxides	$M_2Zr_2O_7$-type structure; $(LaCeNdSmEu)_2Zr_2O_7$: κ(300 K) = 0.76 W m^{-1} K^{-1}, 70% grain growth rate reduction versus $La_2Zr_2O_7$; $(\{RE\})_2Zr_2O_7$: κ(300–1200 °C) < 1 W m^{-1} K^{-1}	104,105
2019	(HfNbTaTiZr)C	fcc lattice, porosity = 80.99%, compressive strength = 3.45 MPa, κ = 0.39–0.49 W m^{-1} K^{-1}	32
Thermoelectrics			
2018	(AgBiGe)Se	fcc lattice, κ = 0.43 W m^{-1} K^{-1}, power factor (773 K) = 3.8 μW cm^{-1} K^{-2}, ZT(677 K) = 0.45	138
2018	$(Cu_5GeMgSnZn)S_9$	Tetragonal lattice, κ = 1.0–1.9 W m^{-1} K^{-1}, power factor (773 K) = 8 μW cm^{-1} K^{-2}, ZT(723 K) = 0.58	19

C_f, carbon fibre; CO, carbon monoxide; CO_2, carbon dioxide; EFA, entropy-forming ability; fcc, face-centred cubic; hcp, hexagonal close packed; *M*, metal; *RE*, rare-earth metal; *TM*, transition metal; *ZT*, thermoelectric figure of merit. Electronic properties: *C*, specific capacitance; E_{gap}, band gap; *I*, specific current; ϵ_r, dielectric constant. Magnetic properties: T_N, Néel temperature. Mechanical properties: *E*, elastic modulus; *H*, hardness. Thermal properties: α, coefficient of thermal expansion; κ, thermal conductivity.

Standard ab initio techniques, generally unreliable with ceramics as the chemical character of the constituents differs substantially, have been empirically corrected[46,47], facilitating quantitative analyses.

Reciprocal high-entropy ceramics have distinct cation and anion sublattices, which can offer independent solubilities and stabilizations[48]. The anions screen the metal cations from each other and ease the introduction of further configurational disorder[13], increasing the number of compositions forming single phases and the stability ranges.

Understanding operating conditions is critical for continued development. This involves parameterizing miscibility gaps and melting temperatures[49,50]. Whereas the impact of entropy is unavoidable[48], its intricacies must be addressed: the competition between enthalpy and entropy as a function of the increasing number of species (N) dictates the accessibility of synthesizable states (the so-called '$N+1$ theorem', discussed in BOX 1)[15,48].

Prior to the synthesis of entropy-stabilized oxides, high-entropy ceramics were first explored as thin-film analogues to disordered metal alloys. Early attempts to synthesize high-entropy nitride thin films employed magnetron sputtering of high-entropy alloy targets in an $Ar + N_2$ atmosphere, and resulted in amorphous or multiphase films[51,52]. (AlCrTaTiZr)N was the first composition to form a single-phase crystalline structure[42]. Oxide thin-film AlCoCrCuFeNi followed thereafter[53,54]. These systems, important predecessors to present-day

Box 1 | Entropy stabilization

Entropy stabilization was first demonstrated in 2015 with the synthesis of an equimolar mixture of MgO, CoO, NiO, CuO and ZnO forming single-phase (MgCoNiCuZn)O with a rock-salt structure[13] (FIG. 2a). The limited solubilities of MgO–ZnO and CuO–NiO and the structural mismatches with tenorite CuO and wurtzite ZnO were overcome by entropy (by increasing the number of species (N): $N \rightarrow N+1$ (REFS[15,48])). Subsequent reports[55,73,76,192] corroborated the original finding that entropy controls the transition from a multiphase to a single-phase state: the transition is endothermic and reversible with temperature; removing any component oxide — and reducing the configurational entropy — yields a multiphase system in the absence of a post-annealing treatment[36,55,73,76]; and the transition temperature increases as the relative cation ratios deviate from equimolarity, where the number of configurations is maximum (multidimensional eutectoid).

Entropy promotion is mediated by the chemically ordered anion sublattice through two complementary phenomena: the anion sublattice produces almost indistinguishable nearest-neighbour environments for the cations, enhancing energetic degeneration and thus increasing entropy[13]; and the sublattice can deform to accommodate differences in cation sizes and bonding (an energetically expensive process in metal alloys)[8], mitigating their enthalpic penalties[55] and producing a cation sublattice with as little distortion as possible[60,61,66]. The overall outcome is the suppression of clustering and segregation and a homogeneous distribution of species[193]. Particular choices of cations may further reduce site distortions. For example, in transition-metal oxides, distortions of d^0 cations (such as Ti^{4+}, V^{5+}, Zr^{4+}, Nb^{5+} and Mo^{6+}) have the smallest energy penalty, allowing other, more sensitive sites (such as Ni^{2+}) to minimize their deformations[194].

Unavoidable disorder. The '$N+1$ theorem'[48] (illustrated in the figure, panel **a**) shows the onset of entropic promotion as a function of the number of miscible species for metallic compounds in the AFLOW.org repository. The enthalpy gains from increasing the number of species in the compound, $\Delta H[N|\{1, \ldots, N-1\}]$, is defined as the energetic distance of the N-species compound from the $\{1, \ldots, N-1\}$ convex-hull hypersurface, a recursive factorization of the formation enthalpy. The percentages indicate the fraction of alloy systems that form ordered compounds (or elements in the case of $N = 1$). With increasing N, $\langle \Delta H[N|\{1, \ldots, N-1\}] \rangle$ decreases due to the presence of fewer compounds with any enthalpy gain,

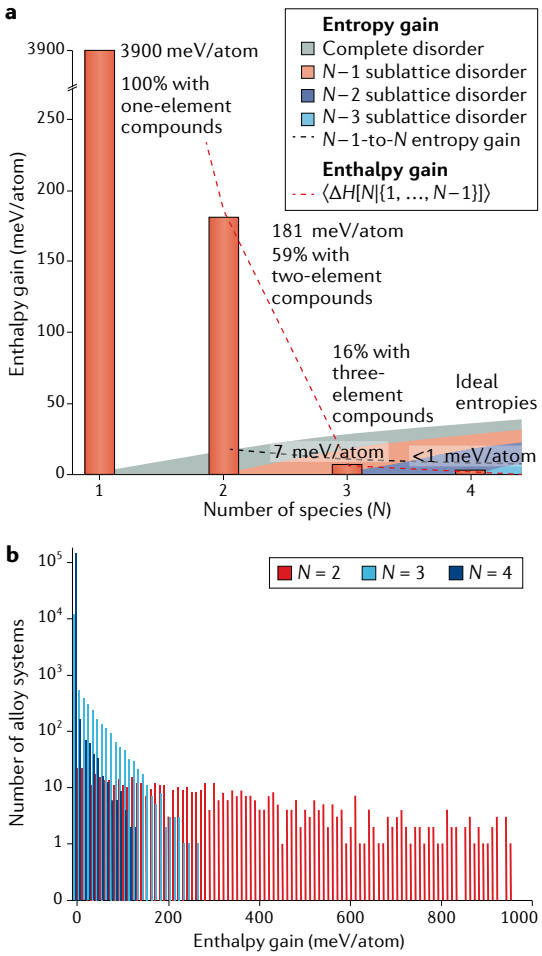

each having a smaller gain (see the figure, panel **b**). The tapering enthalpy gains are surpassed by entropy, with a threshold dependent on whether the disorder is isolated to particular sublattices (reciprocal systems) and on the bonding type (for example, metals versus ceramics). The transition from ordered compounds to high-entropy systems and then entropy-stabilized systems is unavoidable.

high-entropy ceramics, are discussed in 'Disordered thin films'.

This Review is organized as follows. The concept of entropy stabilization (unavoidability of disorder) is summarized first, followed by an overview of theoretical studies for synthesizability and properties prediction. Then, several material chemistries (oxides, borides, carbides, nitrides and silicides) are introduced together with the applications already explored (batteries, supercapacitors, thermoelectrics, catalysis, thermochemical water splitting, and thermal and environmental protection). Disordered thin films are then discussed for wear-resistant, corrosion-resistant and biocompatible coatings, microelectronic diffusion barriers, electronic ceramics, spintronic layers and thermal insulators. We conclude with future directions and opportunities for high-entropy ceramics in terms of applications, chemistries and methods.

Computational investigations

Synthesizability. Computational studies contributed to the understanding of high-entropy oxides, carbides and borides. Classical simulations have explored the competition between enthalpy and entropy and its role in stabilizing (MgCoNiCuZn)O and its derivatives, and have highlighted the disruptive role of Cu on the lattice[55]. Formation enthalpies of multicomponent carbides[56] were determined with density functional theory calculations of special quasirandom structures (SQS)[57]. Such calculations, combined with the ideal configurational entropy approximation, were used to estimate the order–disorder transition temperatures and to determine appropriate synthesis conditions[58]. Unfortunately, this method tends to underestimate the required sintering temperature, because the ideal entropy approximation assumes that all possible configurations are accessible, which is not always the case (SQS structures are optimized to represent an infinite temperature expansion of configurational disorder).

A computational descriptor of entropy-forming ability was developed[15] to address the synthesizability of high-entropy carbides based on the energy distribution of small disordered configurations[15,45] (representing a tuneable-temperature ensemble expansion of the system)[59]. The descriptor was used to correctly predict the synthesis of six new high-entropy carbides with a rock-salt structure, produced using high-energy ball-milling and spark plasma sintering (SPS), and the decomposition of three other systems. In particular, the composition of the system with the highest entropy-forming ability, (MoNbTaVW)C (150 meV/atom above the convex hull), was counter-intuitive: it could hardly have been predicted using empirical or phenomenological rules because two of the precursors, Mo_2C and W_2C, do not share the cubic structure of the others. The hardness values of these carbides generally exceed those expected from the rule of mixtures and computational predictions, suggesting solid-solution strengthening and/or changes in slip planes. The supercell ensemble approach[59] offers complementary insight to SQS, particularly for disorder in the finite temperature regime.

Properties. SQS calculations were performed to study the charge compensation mechanism involved in the incorporation of a sixth cation in (MgCoNiCuZn)O (REF.[60]). The results corroborated the presence of a Cu-induced Jahn–Teller distortion and revealed its nature and, more generally, the structure of the oxygen sublattice[60–62]. Feedback between experiments and simulations has been especially beneficial in understanding the charge compensation among cations[60,63–65] and Jahn–Teller behaviour[60–62,66]. The amorphous-like thermal conductivity of (MgCoNiCuZn)O and derivatives was examined with an experimentally fitted virtual crystal approximation and molecular dynamics simulations[41]. Molecular static calculations revealed that substitutions by Li or Mn introduce weaker ionic interactions that make (MgCoNiCuZn)O more compressible, affecting its potential application in catalysis and batteries[30]. An approach combining defect chemistry and CALPHAD[67,68] (the 'CALculation of PHAse Diagrams' method, which leverages available experimental and theoretical data to construct models for the Gibbs free energy and resolve phase boundaries)[67,68] was used to investigate and visualize how control parameters affect the mixing behaviour of perovskite oxides[69]. SQS and other supercell-based calculations have also been employed to investigate the thermomechanical and electronic properties of borides[70] and carbides[15,56,58,71]. The non-zero electronic density of states at the Fermi level indicates metallicity[15,56,70,71], whereas the electronic charge distribution suggests covalent bonding with some ionic contribution[56,71]. Elasticity calculations demonstrate that the materials are brittle, although a brittle–ductile transition is predicted for (HfNbTaTiZr)C at 20 GPa (REF.[56]).

Single-phase high-entropy ceramics

The rock-salt (MgCoNiCuZn)O alloy. Much attention has been focused on the synthesis of (MgCoNiCuZn)O and its derivatives (FIG. 2a), with routes including solid-state reaction[13,63,72], nebulized spray pyrolysis[73], flame spray pyrolysis[73], co-precipitation[73–75] and a modified solution combustion synthesis method[76]. There are conflicting reports on whether single-phase (MgCoNiCuZn)O can be achieved with mechanochemical synthesis — ball-milling under ambient conditions — alone, and whether this affects its catalytic performance[77,78]. These two studies used different cobalt oxide precursors: rock-salt CoO (REF.[77]) and spinel Co_3O_4 (REF.[78]). Both studies led to single-phase rock-salt (MgCoNiCuZn)O at high temperatures[13,63], suggesting that the heat treatment is necessary to overcome the structural mismatch. A separate study incorporated LiF into (MgCoNiCuZn)O via mechanochemical synthesis and noted that some amorphous material may form as well[38].

The entropy-stabilizing nature of the anion sublattice invites the incorporation of additional cation species, further promoting entropy stabilization. All of the cations in (MgCoNiCuZn)O are in a 2+ valence state[63]. Feasible additions include aliovalent substitutions by 1+ elements (Li (REF.[63]), Na and K (REF.[64])) and co-substitutions by 1+ and 3+ elements (Li and Ga)[63], enabled by two charge-compensation mechanisms: a change in the valence state of the cations (such as

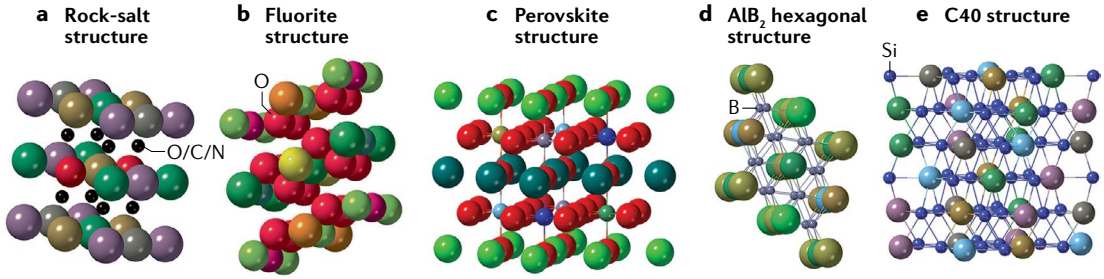

Fig. 2 | **High-symmetry structures of high-entropy ceramics.** Structures and compositions include the rock-salt structure (space group $Fm\bar{3}m$ #225, AFLOW (Automatic Flow Framework for Materials Science)[93] prototype label[94,95] AB_cF8_225_a_b) (oxides, carbides, nitrides) (part **a**), the fluorite structure ($Fm\bar{3}m$ #225, AB2_cF12_225_a_c) (oxides) (part **b**), the perovskite structure ($Pm\bar{3}m$ #221, AB3C_cP5_221_a_c_b) (oxides) (part **c**), the AlB_2 hexagonal structure ($P6/mmm$ #191, AB2_hP3_191_a_d) (borides) (part **d**) and the C40 structure ($P6_222$ #180, AB2_hP9_180_d_j) (silicides) (part **e**).

Co^{2+} to Co^{3+})[60,63–65] and/or the formation of oxygen vacancies[63–65]. Substitutions by other oxide-forming elements (Ca, Sc, Cr, Ge, Sn and Sb) are feasible in thin films, as discussed in the section Disordered thin films[60,79]. Among viable substitutions, Li incorporation has been a major focus, yielding a colossal dielectric constant ($\epsilon_r \approx 2 \times 10^5$)[63] and room-temperature superionic Li conductivity ($>10^{-3}$ S cm^{-1})[64], exceeding that of the commonly used solid electrolyte LiPON (lithium phosphorus oxynitride)[80] by more than two orders of magnitude.

Among the cations of (MgCoNiCuZn)O, Cu is the most anomalous. Cu is responsible for Bragg peak intensities, widths and shapes deviating from those of an ideal rock-salt structure[66,81]; Cu exhibits a tendency for cluster formation and phase separation into tenorite CuO (≤800 °C) and Cu_2O (≥1100 °C)[13,55,72,82] with different heat treatments and quench conditions[83]; Cu yields a large distortion of the anion sublattice[55,61,66,81]; an increasing Cu concentration lowers the high-spin Co^{2+} fraction (converting it to low-spin Co^{3+}) and reduces the strength of the antiferromagnetic interaction in the system[81]; and CuO is the slowest oxide to incorporate into the single-phase structure[82]. The anomalies stem from size-related effects[55] and Jahn–Teller behaviour[60,61,66]. Structural deformations are not cooperative (that is, elongated in the same direction) and include both tetragonal elongation and compression, often also showing slight orthorhombic distortion[62,66]. The Jahn–Teller compression accounts for about 10% of distortions and is unexpected, likely reflecting the competition between the preferred octahedral environments of other cations with the Cu-centred elongation distortions[62]. These distortions increase with Cu concentration, slower cooling speeds and post-annealing treatments, and have a strong impact on dielectric properties that should be further investigated[66].

Investigations of magnetic ordering in (MgCoNiCuZn)O were first carried out in thin films (see the section Disordered thin films) and were motivated by the antiferromagnetism in three of the five binary oxide constituents: CoO, NiO and CuO (REF.[84]). Magnetic ordering of any kind could not be taken for granted given the strong disorder in the compound, although a spin-glass-like state could be expected[85]. However, (MgCoNiCuZn)O exhibits long-range antiferromagnetic behaviour with a Néel temperature (T_N) in the 106–140 K range[76,85,86]. Such a wide-ranging T_N along with a reduced T_N and ordered magnetic moment — compared with those of its components — suggest a sluggish magnetic transition suppressed by disorder and/or magnetic frustration, as further corroborated by evidence for short-range magnetic fluctuations above the T_N (REFS[85,86]).

Fluorite oxides. Single-phase Ce-based oxides spanning three to seven cations have been synthesized with stoichiometries (Ce{*RE*})$O_{2-\delta}$ (REFS[87,88]) and (HfZrCe)({*M*})$O_{2-\delta}$ (REFS[89,90]), where {*RE*} are rare-earth elements, {*M*} are metals and the value of δ depends on the cation valence[88,90]. The systems with three to six cations have a CaF_2-type fluorite structure (FIG. 2b), matching that of CeO_2 (REFS[87–90]). The seven-cation compound forms a lower symmetry cubic structure (space group $Ia\bar{3}$ #206) after additional calcination, matching the space group of bixbyite Y_2O_3 (REFS[87,88]). The components of (Ce{*RE*})$O_{2-\delta}$ do not form single phases without Ce, and thus are not entropy-stabilized[87,88]. Conversely, (HfZrCeTiSn)O_2 shows evidence of entropy stabilization: the transition from the multiphase to the single-phase state is reversible[90]. SPS of (HfZrCe)({*M*})$O_{2-\delta}$ compounds results in annealed densities as high as 100%[89].

The optical properties of (Ce{*RE*})$O_{2-\delta}$ compositions have been investigated, revealing narrow band gaps — narrower than those of any of the binary rare-earth oxides or even of many doped rare-earth oxides — enabling light absorption over the full visible spectral range[88]. The multivalent state of Pr (mixed 3+/4+) plays the dominant role in the observed band-gap narrowing. The heavy dependence of stability and gap narrowing on Ce and Pr, respectively, reflects the compositional variability of the systems and offers flexibility for properties engineering.

Perovskite oxides. Materials with perovskite structure are the first examples of high-entropy materials having at least two cation sublattices[91]. Two sets of chemistries were reported. In the first set, the ({Sr,Ba})({*M*})O_3 compositions (FIG. 2c) are synthesized with a total of six[91] and seven[91,92] cations. Thirteen combinations are examined in REF.[91], with six forming single-phase systems; and for these, the Goldschmidt tolerance factors — a dimensionless quantity used to predict the stability of ionic systems,

$t = (r_A + r_O)/\sqrt{2}\,(r_B + r_O)$, where r_A, r_B and r_O are the average ionic radii of the *A* cations, *B* cations and the anion (oxygen in this case), respectively — are all close to unity. Conversely, six of the seven non-homogeneous phases have $t \leq 0.97$ or $t \geq 1.03$. Thus, having $t \approx 1.00$ has been suggested to be a necessary, but not sufficient, condition for forming single phases, whereas cation size differences do not seem to play an important role[91]. For the Ba-containing homogeneous compositions, the precipitation of a Mn-enriched secondary phase — occurring with increasing temperature — casts doubt on their entropy stabilization. In the second set of chemistries, 6-cation and 10-cation[27] $(\{RE\})(\{TM\})O_3$ systems (space group *Pbnm* #62, AFLOW (Automatic Flow Framework for Materials Science)[93] prototype[94,95] AB3C_oP20_62_c_cd_a), where {*TM*} are transition metals, have shown some entropy stabilization: the 10-cation system is homogeneous, whereas five of the six-cation systems are not; and $(GdLaNdSmY)MnO_3$ exhibits a reversible transformation from multiphase to single phase upon cyclic heat treatments[27]. Possible Jahn–Teller distortions in Mn-based systems can prevent the synthesis of homogeneous phases at lower temperatures (<900 °C)[27]. The formation of orthorhombic perovskites — and their preservation at high temperatures — rather than of their cubic counterparts may be driven by enthalpic factors (such as cation-size-related distortions, preferred oxidation states of elements and Jahn–Teller behaviour) and should be examined further. Magnetic ordering has also been investigated in rare-earth-based perovskites[96]. The $(\{RE\})(CoCrFeMnNi)O_3$ compounds exhibit a complex magnetic state dominated by antiferromagnetic interactions. Superexchange coupling within the transition metal cation sublattice yields competing antiferromagnetic and ferromagnetic interactions. It has been proposed that small ferromagnetically coupled clusters order at high temperatures and lock into a gradually ordering antiferromagnetic matrix upon cooling[96]. Despite the complex state, the magnetic ordering temperatures (110–180 K) correlate well with the size of the rare-earth ions (Goldschmidt tolerance factor). Non-Curie–Weiss behaviour in $La(CoCrFeMnNi)O_3$ — also observed in (MgCoNiCuZn)O — indicates the presence of magnetic correlations above the T_N.

Other oxides. Various other oxide systems have been realized, including: ferrimagnetic $(CoCrFeMnNi)_3O_4$ (REFS[97,98]) and ferromagnetic $(CoCrFeMnZn)_3O_4$ and $(CoCrFeNiZn)_3O_4$ (REF.[99]) spinel compounds (space group $Fd\bar{3}m$ #227, AFLOW prototype[94,95] A3B4_cF56_227_ad_e); magnetoplumbite $BaFe_6(TiCoInGaCr)_6O_{19}$ (REFS[100,101]); bixbyite $(GdTbDyHoEr)_2O_3$ (REF.[102]) ($Ia\bar{3}$ #206, AB3C6_cI80_206_a_d_e); rare-earth silicates[28,29,103]; cubic metal pyrophosphate $(TiZrHf)P_2O_7$ (REF.[31]); six-cation pyrochlore $(\{La,Ce,Nd,Sm,Eu,Gd,Y\})_2Zr_2O_7$ (REFS[104,105]) ($Fd\bar{3}m$ #227, A2B2C7_cF88_227_c_d_af); and amorphous spheres of $10La_2O_3$–$20TiO_2$–$10Nb_2O_5$–$20WO_3$–$20ZrO_2$ (REF.[106]).

Unlike other high-entropy oxides, bixbyite $(GdTbDyHoEr)_2O_3$ exhibits a non-reversible transformation to a single phase, suppressing the phase transformation occurring in its single-cation counterparts[102]. Because the system maintains a homogeneous, single-phase, solid-solution state from room temperature to 1650 °C, quenching and the associated cracking can be avoided during production.

Borides, carbides, nitrides and silicides. Bulk high-entropy borides, carbides, nitrides, carbonitrides, borocarbides and silicides (TABLE 1) have been synthesized using approaches such as SPS[14–16,20,21,45], boro/carbothermal reduction of metal oxides (which has the advantage of producing finer powders, which aid in densification)[32,107–114] and a low-temperature mechanically induced self-sustaining reaction[115]. These materials often display enhanced hardness, above that predicted from the rule of mixtures[14–16,45], due to solid-solution hardening or changes in the availability of lattice slip systems[16]. Like (MgCoNiCuZn)O, carbides and nitrides typically form on the rock-salt structure (FIG. 2a). Borides typically form on the AlB_2 hexagonal structure (FIG. 2d) with alternating 2D boride and high-entropy cation layers, whereas the silicides form relatively low-symmetry structures based on the C40 crystal structure (FIG. 2e) for $(MoNbTaTiW)Si_2$ (REF.[20]) and on a hexagonal structure (space group $P6_222$ #180) for $(MoNbTaWZr)Si_2$ (REF.[21]).

Applications

Lithium-ion batteries. The superionic conductivity observed in (MgCoNiCuZn)O (REF.[64]) sparked subsequent investigations of this material for use in Li-ion batteries[36,37,116,117]. As an anode (negative electrode) material[116], (MgCoNiCuZn)O delivers high Li storage-capacity retention and good cycling stability that improves with particle-size reduction[36,116]. For reference, transition-metal binary oxides offer limited capacity retention and efficiency[36,116], and four-cation variants — which require post-annealing treatment to be synthesized — suffer from stability and performance deficiencies[36]. The cycling stability is likely a result of the preservation of the rock-salt structure throughout the entire redox process, in which some of the cations (such as Co and Cu) participate in the conversion reactions while others (such as Mg) keep the structure intact[36] and suppress active nanograin aggregation[116]. The ability to introduce defects during conversion reactions without inducing phase separation is attributed to entropy stabilization, that is, thermodynamic preference for the homogeneous five-cation system. As a practical application, full cells with a $LiNi_{1/3}Co_{1/3}Mn_{1/3}O_2$ (NCM111) cathode (positive electrode) were assembled[117]. Pouch cells were also built and employed to power 32 light-emitting diodes[117].

Through the incorporation of both lithium and fluorine, (MgCoNiCuZn)O can also serve as a lithium source, that is, as cathode active material[38]. Oxyfluorides are important electrode materials for their ability to suppress oxygen loss during cycling, with fluorine offering resistance against hydrogen fluoride etching. X-ray diffraction corroborates the formation of a rock-salt phase with lithium and fluorine atoms randomly distributed on the cation and anion sublattices, respectively. A reversible transformation from a multiphase to a single-phase state indicates entropy stabilization.

$Li_x(MgCoNiCuZn)OF_x$ exhibits a working potential of 3.4 V versus Li^+/Li, compared with ~1.0 V for (MgCoNiCuZn)O, promoted in part by a change in the (de)lithiation mechanism from a conversion-type to an insertion-type reaction. It delivers higher reversible specific capacities than rock-salt LiNiOF despite a decrease in the redox-active ion fraction. Access to more mobile Li — otherwise contributing to structural stability in other materials — may play a role in enhancing the reversible capacity. $Li_x(MgCoNiCuZn)OF_x$ also achieves high retention of coulombic efficiencies. Just as in (MgCoNiCuZn)O, the cycling stability is attributed to entropy stabilization, which may help counteract degradation due to oxygen release. The synthesis of its sodiated counterpart $Na_y(MgCoNiCuZn)OCl_y$ might pave a way towards the design of post-lithium battery technologies[38].

(MgCoNiCuZn)O has also been investigated as a polysulfide anchor (functional catalyst) for the sulfur cathode in lithium–sulfur batteries, mitigating the shuttle effect caused by the dissolution of lithium polysulfides in the electrolyte and diffusion back and forth between the electrodes[37]. The interaction between (MgCoNiCuZn)O and lithium polysulfides creates Li–O and S–Ni bonds contributing to the immobilization of lithium polysulfides in the sulfur electrode. Coin cells employing (MgCoNiCuZn)O as a polysulfide anchor exhibit competitive reversible capacity, outstanding cycling stability and low capacity decay.

Supercapacitors. The high-entropy nitride (CrMoNbVZr)N (REF.[18]) has been investigated for use in supercapacitor applications. (CrMoNbVZr)N was synthesized using a mechanochemical soft urea approach, and had specific capacitances ranging from 230 to 54 $F\,g^{-1}$ for scan rates between 10 and 200 $mV\,s^{-1}$. The value 78 $F\,g^{-1}$ measured at a scan rate of 100 $mV\,s^{-1}$ is substantially higher than the value of 46.9 $F\,g^{-1}$ measured for VN@C (carbon-coated vanadium nitride nanowire)[118] electrodes under the same conditions.

Thermochemical water splitting. (MgCoNiCuZn)O inspired the development of the $(MgCoNiFe)O_x$ ($x \approx 1.2$) polycation oxide, which leverages a mixed solid-phase state (rock-salt and spinel) to perform two-step thermochemical water splitting at reduction temperatures relevant for modern large-scale chemical infrastructures (≤1100 °C)[119]. $(MgCoNiFe)O_x$ outperforms state-of-the-art materials in several capacities: H_2 yields of 10.1 ± 0.5 ml-H_2 g^{-1} at 1300 °C and 1.4 ± 0.5 ml-H_2 g^{-1} at 1100 °C, whereas ceria and spinel ferrites require >1300 °C to yield appreciable H_2; better resistance to H_2 oxidation reverse reaction during water splitting than Mn-based perovskites; and almost no performance degradation over 10 cycles for both temperature conditions, likely a result of high mixing entropy preventing phase separation into binary oxides.

Catalysis. For catalysis, high-entropy metal alloys have been studied for a while[7] and have been shown to possess useful qualities, including: corrosion resistance, which limits traditional transition metal alloys as electrocatalysts in acidic or alkaline environments[120]; resistance to poisoning[121]; a large number of unique binding sites providing a nearly continuous distribution of adsorption energies[122,123]; synergetic and/or unexpected activity enhancements[120–122]; and increased miscibility of elements allowing the optimization of binding strength for higher activity[123–125]. Indeed, high-entropy alloys have been proven to be effective in several reactions, such as oxidation (methanol[121,126,127], ammonia[128], carbon monoxide[127]), evolution (oxygen[124], hydrogen[120,127]), decomposition (ammonia[125]), reduction (oxygen[122,123,127]) and degradation (azo dye)[129].

The combination of bond chemistries in high-entropy ceramics can lead to promising avenues for catalysis. Three recent sets of reports are relevant. In the first, precious-metal-loaded (MgCoNiCuZn)O was investigated for CO oxidation[74] and CO_2 hydrogenation[77]. The disordered oxide was found to promote highly dispersed Pt/Ru up to 5 wt.%, enhancing activity, and to offer resistance to precious-metal sintering during high-heat treatments (up to 900 °C for CO oxidation and 700 °C for CO_2 hydrogenation) and at reaction temperatures (CO was completely converted at 155 °C over the Pt-loaded catalyst, which retained good reusability). At a reaction temperature of 500 °C, CO yields and CO_2 conversions of over 45% were reported for 5 wt.% Pt/Ru-loaded catalysts. CO selectivities for Pt/Ru-loaded CO_2 hydrogenation catalysts were over 95%[77]. In the second set of reports, mesoporous $(MgCoNiCuFe)O_x$–Al_2O_3 was investigated for CO oxidation[130]. Complete CO conversion occurred at 260 °C. The ceramic exhibited negligible degradation after 48 h[130], and superior sulfur tolerance to CuO–Al_2O_3. In the third set of reports, systems containing nitrogen, carbon, oxygen and boron were identified as promising candidates for oxygen reduction[122,131–136].

Despite the good activity of such systems, performance improvements are needed to compete with platinum and state-of-the-art alloys. High-entropy ceramics may present an optimal intersection of critical properties, especially in non-trivial geometries[121,131] and/or if their pore structure is tuned[132] to enhance their surface area. Given their promising properties, we foresee a plethora of studies on catalysis based on high-entropy ceramics in the coming years.

Thermal and environmental protection. (MgCoNiCuZn)O exhibits amorphous-like thermal conductivity — low values increasing with temperature — without compromising its mechanical stiffness, a common trade-off in non-metals, in which phonons are the dominant heat carriers[41]. Rayleigh scattering (rather than momentum-destroying Umklapp processes) was found to be the dominant phonon scattering mechanism dictating thermal conductivity in high-entropy ceramics. The thermal conductivity can be further reduced with the addition of a sixth cation (Sc, Sb, Sn, Cr or Ge), which is possible in thin films grown by pulsed laser deposition[13,41,60,79,84]. The resulting drop in thermal conductivity by a factor of two is largely independent of mass, but driven instead by local ionic charge disorder, which strains the oxygen sublattice and induces large variations in the interatomic

force constants[41]. High-entropy oxides exhibit ratios of elastic modulus to thermal conductivity among the highest reported at room temperature, exceeding those of prominent thermal barrier coatings, such as zirconate materials[41] (TABLE 2).

Other high-entropy oxides possess attractive thermomechanical properties. (HfZrCe)({*M*})$O_{2-\delta}$ compounds have Vickers hardness comparable with that of 8 mol.% Y_2O_3-stabilized ZrO_2 (the standard thermal barrier coating 8YSZ (REF.[137])) and higher than that of many doped zirconia-based and ceria-based ceramics, despite high contents of the soft components Y_2O_3 and Yb_2O_3 (REF.[89]). The fluorite systems also have lower thermal conductivities (1.1–1.81 W m^{-1} K^{-1}) than 8YSZ (2.02 ± 0.17 W m^{-1} K^{-1})[89,90]. Pyrochlore and metal pyrophosphate compounds have room-temperature thermal conductivities lower than 1 W m^{-1} K^{-1} (REFS[31,104,105]), which pyrochlores can maintain up to 1200 °C (REF.[105]). These values are lower than those for single-cation rare-earth zirconates $RE_2Zr_2O_7$ (1.2–1.9 W m^{-1} K^{-1}), YSZ (1.7–1.9 W m^{-1} K^{-1}) and single-cation transition metal pyrophosphates TMP_2O_7 (0.8–1.1 W m^{-1} K^{-1})[104].

Beyond thermal stress, aggressive turbine environments corrode Si-based ceramic matrix composites without the protection of robust coatings. Single-cation rare-earth silicates have been investigated, but generally fall short in incorporating all necessary mechanical, thermal and chemical properties. The high-entropy compounds $(YbYLuScGd)_2Si_2O_7$ (REF.[28]) (space group *C*2/*m* #12, AFLOW prototype[94,95] A7B2C2_mC22_12_aij_h_i) and $(YHoErYb)_2SiO_5$ (REF.[29]) exhibit a cocktail of critical features often exceeding those predicted by the rule of mixtures: good phase stability, coefficients of thermal expansion well matched with those of Si-based ceramics and excellent resistance to water-vapour corrosion. $(YbYLuScGd)_2Si_2O_7$ has the highest residual flexural strength and a strength retention on a par with or better than that of single-cation disilicates under a corrosive environment of 50% H_2O–50% O_2 at 1250 °C for 300 h. $(YHoErYb)_2SiO_5$ has a higher elastic modulus over the 300–1600 K temperature range than its single-cation counterparts. Its low coefficient of thermal expansion is attributed to the high elastic stiffness, which provides resistance to internal thermal pressure, and to two competing phonon species enabling engineering of the thermal expansion behaviour. Monoclinic-phase $(YbYLuEr)_2SiO_5$ has strong anisotropy in its coefficient of thermal expansion, which enables the minimization of the coating/substrate mismatch through the control of its preferred orientations[103].

Highly porous (80.99%) samples of (HfNbTaTiZr)C with very low thermal conductivity were synthesized using carbothermal reduction[32]. Their compressive strength was 3.45 MPa. Their thermal conductivity was 0.39 W m^{-1} K^{-1} at 25 °C, increasing to 0.49 W m^{-1} K^{-1} at 200 °C, approximately 20 times smaller than the value of 6.45 W m^{-1} K^{-1} for non-porous (HfNbTaTiZr)C. The sample was stable under thermal cycling to 1850 °C, with X-ray diffraction showing the same single-phase rock-salt structure throughout, indicating high thermodynamic stability.

Thermoelectrics. Their reduced lattice thermal conductivity makes high-entropy semiconductors promising materials for thermoelectric applications. The performance of Cu–S-based high-entropy materials was investigated by synthesizing $Cu_5SnMgGeZnS_9$ and $Cu_3SnMgInZnS_7$ using ball-milling and SPS[19]. A thermoelectric figure of merit (*ZT*) of 0.58 at 723 K was measured for the composition $Cu_5Sn_{1.2}MgGeZnS_9$, similar to the values for ordered ternary and quaternary diamond-like sulfides. Little improvement was obtained by introducing disorder, most likely due to the already low thermal conductivity of Cu–S materials. A more promising approach might be the introduction of disorder into materials that have the potential of becoming good thermoelectrics if their thermal conductivity can be lowered.

The high-entropy selenide (AgBiGe)Se was synthesized by a melting reaction of GeSe and $AgBiSe_2$ in a sealed vacuum tube[138], forming a homogeneous rock-salt structure for 50% $AgBiSe_2$. Its power factor was 3.8 μW cm^{-1} K^{-2} at 677 K, and its thermal conductivity was 0.43 W m^{-1} K^{-1} at 300 K. *ZT* reached a maximum of 0.45 at 677 K.

Disordered thin films

High-entropy nitride, carbide, boride and oxide thin films have been deposited on Si, steel, Ti6Al4V alloy, quartz glass, WC–Co cemented carbide, MgO and $SrTiO_3$ substrates using sputtering of elemental or high-entropy alloy targets in an Ar + N_2, Ar + CH_4 or Ar + O_2 atmosphere, as well as using a cathodic arc and pulsed laser deposition. Pulsed laser deposition expands the solubility of cations by contributing an 'effective temperature' via incident particle kinetic energy, enabling the incorporation of Ca, Sc, Cr, Ge, Sn and Sb[60,79]. High-entropy ceramic films have been investigated for potential use as wear-resistant, corrosion-resistant and/or oxidation-resistant coatings, diffusion barriers for microelectronics, electronic ceramics, biocompatible coatings, antiferromagnetic layers for spintronics and thermal insulators (TABLE 2).

The first nitride films were based on high-entropy alloys forming on body-centred cubic or face-centred cubic (fcc) lattices: the films tended to be amorphous or multiphase, not forming the single-phase crystalline solid solutions that characterize high-entropy alloys[51,52]. This was attributed to the presence of metals that do not form nitrides, such as Cu, leading to the formation of separate metallic phases. Using good nitride formers, such as Al, Cr, Ta, Ti and Zr, leads to the formation of single-phase fcc solid-solution films[42]. Hexagonal AlN, in particular, dissolves easily into the fcc lattice, with (AlTi)N solid solutions having an fcc lattice up to ~60% AlN, and Al enhancing the oxidation resistance of coatings. Similar to nitrides, high-entropy oxides were originally explored as thin films of high-entropy alloys (metals) deposited at high oxygen pressures, often yielding high-symmetry structures, such as hexagonal close packed[53], spinel[54] and fcc[139–141].

Wear-resistant, corrosion-resistant and oxidation-resistant coatings. High-entropy carbides, nitrides, carbonitrides and oxides display enhanced hardness due to

Table 2 | **High-entropy ceramics for thin-film materials applications**

Year	Material	Description	Refs
Wear-resistant and corrosion/oxidation-resistant coatings			
2006	(AlCrTaTiZr)N	fcc lattice, H = 28.5–36.9 GPa, E = 368 GPa, μ = 0.76, wear rate ≈ 6.5–3.66 × 10^{-6} mm^3 N^{-1} m^{-1}, oxidation temperature = 800 °C, increases to >1000 °C with Si addition	39,42,165
2007	Al_2(CoCrCuFeNi)O	Spinel structure, H = 22.6 ± 1.6 GPa, E_{gap} = 1.56–1.68 eV	54
2007	(AlCrSiTiV)N	fcc lattice, H = 19–31.2 GPa, E > 300 GPa, corrosion current = 5.37–19.4 μA/cm^2	166,167
2008	(AlCrMoSiTi)N	fcc lattice, H = 15–34 GPa, E = 200–380 GPa	168
2009	(AlCrNbSiTiV)N	fcc lattice, H = 35–41 GPa, E = 300–360 GPa, μ = 0.179–0.265, corrosion current = 0.247–0.346 μA/cm^2	169,170
2010	(AlCrTaTiZr)O	Crystallizes at 900 °C (mixed phase), H ≈ 20 GPa, E ≈ 230 GPa, ρ = 10^{12} μΩ-cm	143
2011	(CrHfTiVZr)N	fcc lattice, H = 30–48 GPa, E = 290–316 GPa	171
2011	(AlCrMoTaTiZr)N	fcc lattice, H = 25–40.2 GPa, E = 370–420 GPa, μ = 0.74–0.80, wear rate = 2.8–2.9 × 10^{-6} mm^3 N^{-1} m^{-1}	172
2011	(AlCrTaTiZr)CN	fcc lattice, H = 20–35 GPa, elastic modulus = 242–280 GPa	173,174
2012	(CrTaTiVZr)N	fcc lattice, H = 11.3–36.4 GPa, E = 200.3–273.8, ρ = 131–446 μΩ-cm	175,176
2012	(AlCrSiTiZr)N	Amorphous with fcc nanocrystallites, H = 16–17 GPa, E = 220–230 GPa, corrosion current = 3.1–19.1 μA/cm^2	177
2012	(HfNbTiVZr)N	fcc lattice, H = 36–70 GPa, E = 281–384 GPa, μ = 1.19, wear rate = 0.39 × 10^{-6} mm^3 N^{-1} m^{-1}	178,179
2012	(AlBCrSiTi)N	fcc crystallization at 800 °C, H = 23 GPa, E = 256.6 GPa	180
2012	(HfNbTaTiZr)C	fcc lattice, H = 27.5 GPa, μ = 0.15, wear rate = 0.8 × 10^{-6} mm^3 N^{-1} m^{-1}	142
2012	(HfNbTaTiZr)N	fcc lattice, H = 32.9 GPa, μ = 0.96, wear rate = 2.9 × 10^{-6} mm^3 N^{-1} m^{-1}	142
2013	(CuSiTiYZr)C	Amorphous; H = 20.7–29.5 GPa, μ = 0.15, wear rate = 1.89 × 10^{-6} mm^3 N^{-1} m^{-1}, corrosion current = 0.535–0.841 μA/cm^2	181
2013	(AlCrNbSiTi)N	fcc lattice, H = 16–36.7 GPa, E = 300–450 GPa, good oxidation resistance at 900 °C	40
2013	(AlCrMoTaTi)N	fcc lattice, H = 20.6–30.6 GPa, E = 260–290 GPa, ρ = 536–8212 μΩ-cm, oxidation temperature = 1073 K, increases to >1173 K with Si addition	33,182
2017	(HfNbTaTiVZr)C	fcc lattice, H = 43–48 GPa, E = 337 GPa	183
2018	(CrNbTaTiW)C	fcc lattice (bct for Ta and W rich), H = 11.7 GPa (Nb rich)–35.5 GPa (Ta and W rich), E = 367 GPa (~equimolar)–568 GPa (Ta and W rich)	184
2018	(CrNbSiTiZr)C	fcc lattice, H = 22.3–32.8 GPa, E = 191–358 GPa, μ = 0.07–0.4, wear rate = 0.2–3.3 × 10^{-6} mm^3 N^{-1} m^{-1}	185
2018	(HfTaTiVZr)B_2	H = 47.2 GPa, E = 540.1 GPa	186
Diffusion barriers for microelectronics			
2008	(AlMoNbSiTaTiVZr)N	Amorphous, barrier intact to 850 °C, failure at 900 °C	144
2009	(AlCrTaTiZr)N	fcc nanocrystallites in amorphous matrix, barrier intact to 900 °C	146,187
2012	(AlCrRuTaTiZr)N	Amorphous (4 nm film thickness) or fcc (10^2–10^3 nm film thickness), barrier intact to 800 °C, failure at 900 °C	145,147
2012	(CrHfTiVZr)N	Amorphous (10 nm film thickness) or fcc (10^2–10^3 nm film thickness), barrier intact to 800 °C, failure at 900 °C	188,189
Electronic ceramics			
2011	((Ti/Al)FeCoNi)O	fcc lattice, ρ = 19 μΩ-cm; with Ti: ρ = 28–35 μΩ-cm; with Al: ρ = 18 μΩ-cm	139,140,190
Antiferromagnetic layers for spintronics			
2017	($MgCo_xNiCuZn$)O	fcc lattice, 10-fold exchange-bias enhancement over permalloy/CoO heterostructures	84
Thermal insulators			
2018	(MgCoNiCuZn)O derivatives	fcc lattice, E = 151.0–236.7 GPa, κ = 1.41–1.68 W m^{-1} K^{-1}, volumetric heat capacity = 3.29–3.96 MJ m^{-3} K^{-1}	41
2018	$Ba(ZrSnTiHfNb)O_3$	Perovskite structure, κ = 0.54–0.58 W m^{-1} K^{-1}	148
Biocompatible coatings			
2012	(HfNbTaTiZr)C	fcc lattice, H = 22.4–32.1 GPa, μ = 0.12–0.32, wear rate = 0.2–0.9 × 10^{-6} mm^3 N^{-1} m^{-1}, corrosion current = 0.0287–0.1251 μA/cm^2; biocompatibility similar to Ti6Al4V alloy, replacing Ta or Ti with Si increases cell viability	34,149
2012	(HfNbTaTiZr)N	fcc lattice, H = 30.9 GPa, μ = 0.17, wear rate = 0.29 × 10^{-6} mm^3 N^{-1} m^{-1}, corrosion current = 0.0731 μA/cm^2; biocompatibility similar to that of the Ti6Al4V alloy	149
2016	(NbSiTaTiZr)C	fcc lattice, corrosion current = 0.025 μA/cm^2	191

bct, body-centred tetragonal; fcc, face-centred cubic. Electronic properties: E_{gap}, band gap; ρ, electrical resistivity. Mechanical properties: E, elastic modulus; H, hardness; μ, coefficient of friction. Thermal properties: κ, thermal conductivity.

solid-solution strengthening, as well as good oxidation and corrosion resistance due to their sluggish diffusion, which limits penetration of oxygen and other species (TABLE 2). They are valuable for applications as protective coatings resistant to wear, oxidation and/or corrosion for machine parts, such as cutting tools and drill bits, operating at high temperatures in corrosive environments. Properties including the hardness, elastic modulus, wear rate, coefficient of friction, resistivity, mass gain during annealing in air, and corrosion currents and potentials in corrosive solutions were measured for a range of carbide, nitride and oxide coatings (TABLE 2). Although nitrides are often harder, the corresponding carbides can display a lower wear rate due to their lower coefficients of friction, which can be explained by the formation of a free carbon layer on the surface acting as a lubricant[142]. Al_2(CoCrCuFeNi)O and (AlCrTaTiZr)O films achieve hardness values among the highest exhibited by available oxide coatings; binary oxide films rarely exceed 20 GPa (an exception is Cr_2O_3 with 25–30 GPa)[54,143]. Hardness generally increases with sputtering substrate bias and nitrogen content up to saturation: supersaturated films can develop voids that reduce hardness. Higher aluminium and oxygen concentrations[54] and annealing also enhance hardness, which can be attributed to the incorporation of strong oxygen–metal bonding, elimination of film cracks and voids, and formation of nanocrystalline phases[143].

Diffusion barriers for microelectronic applications. The ongoing miniaturization of microelectronic circuitry down to the nanoscale requires new materials to prevent interdiffusion at the interface between Cu and Si components and the formation of Cu_3Si, which increases electrical resistance, reduces efficiency and interferes with the functionality of the device. Historically, such diffusion barriers have included the SiO_2 native oxide along with nitrides, such as Si_3N_4 and TiN. High-entropy nitrides are particularly promising for such applications, because the lattice distortion and increased packing density resulting from the different elemental radii result in sluggish diffusion even through layers just a few nanometres thick (TABLE 2).

Very thin (~10 nm or less) nitride films on Si substrates typically have an amorphous structure[144,145], often with embedded fcc nanocrystallites[146], in which the lack of grain boundaries helps slow diffusion. Diffusion resistance was investigated by annealing a silicon/nitride/copper stack at temperatures between 400 and 900 °C for ~30 min. The high-entropy nitride barriers generally remained intact up to 800 °C, with transmission electron microscopy measurements showing sharp boundaries between the silicon, nitride and copper layers. Some boundary blurring was observed at 850 °C, with barrier failure leading to Cu_3Si formation and a sharp increase in electrical resistance occurring at 900 °C. The effectiveness of increasing the elemental components to improve the diffusion barrier was demonstrated by a comparison of nitrides with the number of metals ranging from one to six[147]. The failure temperature increased monotonically with the number of elements from 550 °C for TiN to 900 °C for (AlCrRuTaTiZr)N.

Electronic ceramics. Oxidation can have opposite effects on resistivity depending on the alloy system. The resistivity of (AlCrTaTiZr)O films increases with the oxygen concentration (up to 10^{12} μΩ-cm)[143], whereas (TiFeCoNi)O films exhibit their lowest resistivities (35 ± 3 μΩ-cm) after oxidation at high temperatures, which eliminates small voids at amorphous grain boundaries[139]. In fact, the resistivity of (TiFeCoNi)O films continues to decrease with annealing temperatures — dropping below that of bulk TiFeCoNi — even after the resistivity in TiFeCoNi films starts to increase as the films react with the SiO_2/Si substrate forming high-resistivity silicides. The resistivity of (TiFeCoNi)O films is equal to that of single-crystal RuO_2 and lower than that of tin-doped indium oxide thin films (150 μΩ-cm). Although this is still higher than the resistivity of many pure metals, it is low compared with that of ceramic semiconductors at room temperature[139].

Antiferromagnetic layers for spintronics. The antiferromagnetic behaviour of (MgCoNiCuZn)O was first investigated in a heterostructure with ferromagnet permalloy[84]. Exchange coupling at the ferromagnet/antiferromagnet interface can be optimized by balancing the chemical disorder (it is maximum at equiatomic concentrations) and the percentage of magnetic ions (it increases with Co concentration). By tuning the Co concentration, the exchange bias can be enhanced to reach a value an order of magnitude higher than that of permalloy/CoO heterostructures.

Thermal insulators. Six-cation Ba(ZrSnTiHfNb)O_3 thin films, synthesized by pulsed laser deposition, have a thermal conductivity in the 0.54–0.58 W m^{-1} K^{-1} range, almost an order of magnitude lower than that of other single-crystal perovskite oxides having only one or two different elements on the *B* site[148].

Biocompatible coatings. Due to their resistance to wear and corrosion, high-entropy carbides and nitrides are promising materials for coatings for biomedical implants, if they can be demonstrated to be biocompatible and non-toxic. Carbide and nitride coatings showed better corrosion resistance than the bare substrate in simulated body fluid. Biocompatibility was tested using osteoblast[149] or osteosarcoma[34] cells: no cytotoxic responses were observed, with most cells still alive after 72 h. Si-containing coatings were found to improve cell attachment and viability, with (HfNbSiTiZr)C being the most biocompatible material tested[34]. A possible explanation for the improved cell attachment stems from the increased negative surface charge of Si-containing coatings: positively-charged proteins in the solution adhere to the negatively-charged coating, and then attract negatively-charged cells, anchoring them to the surface.

Future directions

The immense compositional space available in high-entropy systems enables property tuning, which is critical if specific responses are required, such as in catalysis or optoelectronics[88], or if the behaviour depends on a combination of interdependent properties, such as in

thermoelectrics. Reciprocal systems, in which independent solubilities of the cation and anion sublattices enable configurational disorder to be present in both, can further enlarge the compositional space in addition to increasing the entropy[48].

The binding strength in catalysts can be optimized — neither too strong nor too weak — by compositional tuning to obtain higher activity under different reaction conditions[123–125]. The variety of binding environments provides a distribution of adsorption energies that can well accommodate reactants and intermediates, including those that would be difficult to use in regular environments[122,123].

Colossal dielectric constants appear to be characteristic of (MgCoNiCuZn)O alloys; the mechanism remains unclear and warrants further study[63,150]. The effect is enhanced by increasing the number of species in the composition: a promising direction for new materials for capacitors and other electronic devices.

The thermoelectric figure of merit depends on the ratio of electrical conductivity and the Seebeck coefficient to thermal conductivity. Disorder lowers the lattice thermal conductivity[41], thus compositions can be selected to optimize the relationship between the Seebeck coefficient and the electronic thermal conductivity to improve the thermoelectric efficiency.

Mechanical properties are highly interdependent: hard, strong materials tend to be brittle, and the wear resistance depends on the ratio of hardness to the elastic modulus[151] and on the friction coefficient[142]. Disorder and microstructural engineering have already been used to optimize the strength-to-ductility ratio in metal alloys[152]; we foresee similar approaches being applied to structural ceramics. Lattice distortion increases the hardness of high-entropy materials, whereas compositional control can be used to adjust the elastic modulus and surface friction to maximize wear resistance.

Many questions remain for computational modelling to address, including the quantitative calculation of the entropy, prediction of transition temperatures, investigation of diffusion rates and better understanding of the mechanisms affecting synthesizability. Methods developed to predict the formation[153] and order–disorder transition temperatures[50] of high-entropy alloys can be extended to ceramics. Entropy can be calculated directly using Monte Carlo simulations[154–156]; this requires energies for many configurations (obtained, for example, using cluster expansion[157,158] or machine learning methods[11,12] trained on ab initio calculations). Molecular dynamics modelling offers clearer insight into kinetic processes in high-entropy ceramics[159], potentially resolving the uncertainty regarding diffusion rates in disordered materials[8,23,25,26]. Modelling will also provide information on the lifetimes of metastable phases under different operating conditions.

Within the high-throughput revolution[10], the vast quantity of computational and experimental information being generated creates opportunities for data analysis and for artificial intelligence and machine learning to identify critical trends for improving both materials design and materials discovery.

Conclusions

Disorder leads to unexpected properties. High-entropy ceramics exhibit remarkable properties orthogonal to those of high-entropy metal alloys, such as high hardness and melting temperatures, persistence of structure in extreme conditions, amorphous-like thermal conductivity, wear and corrosion resistance, and confirmed entropy stabilization.

Disorder enables new applications. Compared with metals, in which electrons are delocalized, ceramics can have pronounced effects originating from disorder-induced charge fluctuations. Potential applications are abundant, amongst them energy storage, water splitting, catalysis, thermoelectricity, electronic device materials, spintronics, thermal and environmental protection, wear resistance and biocompatible coatings. The extension to reciprocal systems, in which configurational disorder also appears in the anion sublattice, further increases entropy and provides a larger compositional space to discover new materials with optimized properties.

The surface of disordered materials has barely been scratched: the immense universe of structures and compositions requires effective joint experimental, theoretical and computational efforts, all simultaneously addressing the synthesizability, stability and applicability of these materials. Entropy is the launch pad for valuable future materials-space explorations.

Published online 12 February 2020

1. Miracle, D. B. High entropy alloys as a bold step forward in alloy development. *Nat. Commun.* **10**, 1805 (2019).
2. Cantor, B., Chang, I. T. H., Knight, P. & Vincent, A. J. B. Microstructural development in equiatomic multicomponent alloys. *Mater. Sci. Eng. A* **375–377**, 213–218 (2004).
3. Yeh, J.-W. et al. Nanostructured high-entropy alloys with multiple principle elements: novel alloy design concepts and outcomes. *Adv. Eng. Mater.* **6**, 299–303 (2004).
4. Feng, R., Liaw, P. K., Gao, M. C. & Widom, M. First-principles prediction of high-entropy-alloy stability. *npj Comput. Mater.* **3**, 50 (2017).
5. Gao, M. C. et al. Computational modeling of high-entropy alloys: structures, thermodynamics and elasticity. *J. Mater. Res.* **32**, 3627–3641 (2017).
6. Widom, M. Modeling the structure and thermodynamics of high-entropy alloys. *J. Mater. Res.* **33**, 2881–2898 (2018).
7. George, E. P., Raabe, D. & Ritchie, R. O. High-entropy alloys. *Nat. Rev. Mater.* **4**, 515–534 (2019).
8. Yeh, J.-W. Recent progress in high-entropy alloys. *Ann. Chim. Sci. Mat.* **31**, 633–648 (2006).
9. Takeuchi, I. et al. Identification of novel compositions of ferromagnetic shape-memory alloys using composition spreads. *Nat. Mater.* **2**, 180–184 (2003).
10. Curtarolo, S. et al. The high-throughput highway to computational materials design. *Nat. Mater.* **12**, 191–201 (2013).
11. Butler, K. T., Davies, D. W., Cartwright, H., Isayev, O. & Walsh, A. Machine learning for molecular and materials science. *Nature* **559**, 547–555 (2018).
12. Schmidt, J., Marques, M. R. G., Botti, S. & Marques, M. A. L. Recent advances and applications of machine learning in solid-state materials science. *npj Comput. Mater.* **5**, 83 (2019).
13. Rost, C. M. et al. Entropy-stabilized oxides. *Nat. Commun.* **6**, 8485 (2015).
14. Gild, J. et al. High-entropy metal diborides: a new class of high-entropy materials and a new type of ultrahigh temperature ceramics. *Sci. Rep.* **6**, 37946 (2016).
15. Sarker, P. et al. High-entropy high-hardness metal carbides discovered by entropy descriptors. *Nat. Commun.* **9**, 4980 (2018).
16. Castle, E., Csanádi, T., Grasso, S., Dusza, J. & Reece, M. J. Processing and properties of high-entropy ultra-high temperature carbides. *Sci. Rep.* **8**, 8609 (2018).
17. Yan, X. et al. $(Hf_{0.2}Zr_{0.2}Ta_{0.2}Nb_{0.2}Ti_{0.2})C$ high-entropy ceramics with low thermal conductivity. *J. Amer. Ceram. Soc.* **101**, 4486–4491 (2018).
18. Jin, T. et al. Mechanochemical-assisted synthesis of high-entropy metal nitride via a soft urea strategy. *Adv. Mater.* **30**, 1707512 (2018).
19. Zhang, R.-Z., Gucci, F., Zhu, H., Chen, K. & Reece, M. J. Data-driven design of ecofriendly thermoelectric high-entropy sulfides. *Inorg. Chem.* **57**, 13027–13033 (2018).

20. Gild, J. et al. A high-entropy silicide: $(Mo_{0.2}Nb_{0.2}Ta_{0.2}Ti_{0.2}W_{0.2})Si_2$. *J. Materiomics* **5**, 337–343 (2019).
21. Qin, Y. et al. A high entropy silicide by reactive spark plasma sintering. *J. Adv. Ceram.* **8**, 148–152 (2019).
22. Senkov, O. N., Miller, J. D., Miracle, D. B. & Woodward, C. Accelerated exploration of multi-principal element alloys with solid solution phases. *Nat. Commun.* **6**, 6529 (2015).
23. Tsai, M.-H. & Yeh, J.-W. High-entropy alloys: a critical review. *Mater. Res. Lett.* **2**, 107–123 (2014).
24. Miracle, D. B. High-entropy alloys: a current evaluation of founding ideas and core effects and exploring nonlinear alloys. *JOM* **69**, 2130–2136 (2017).
25. Grzesik, Z. et al. Defect structure and transport properties in (Co,Cu,Mg,Ni,Zn)O high entropy oxide. *J. Eur. Ceram. Soc.* **39**, 4292–4298 (2019).
26. Miracle, D. B. & Senkov, O. N. A critical review of high entropy alloys and related concepts. *Acta Mater.* **122**, 448–511 (2017).
27. Sarkar, A. et al. Rare earth and transition metal based entropy stabilised perovskite type oxides. *J. Eur. Ceram. Soc.* **38**, 2318–2327 (2018).
28. Dong, Y. et al. High-entropy environmental barrier coating for the ceramic matrix composites. *J. Eur. Ceram. Soc.* **39**, 2574–2579 (2019).
29. Ren, X., Tian, Z., Zhang, J. & Wang, J. Equiatomic quaternary $(Y_{1/4}Ho_{1/4}Er_{1/4}Yb_{1/4})_2SiO_5$ silicate: a perspective multifunctional thermal and environmental barrier coating material. *Scr. Mater.* **168**, 47–50 (2019).
30. Chen, J. et al. Stability and compressibility of cation-doped high-entropy oxide $MgCoNiCuZnO_5$. *J. Phys. Chem. C.* **123**, 17735–17744 (2019).
31. Zhao, Z., Xiang, H., Dai, F.-Z., Peng, Z. & Zhou, Y. $(TiZrHf)P_2O_7$: an equimolar multicomponent or high entropy ceramic with good thermal stability and low thermal conductivity. *J. Mater. Sci. Technol.* **35**, 2227–2231 (2019).
32. Chen, H. et al. High porosity and low thermal conductivity high entropy $(Zr_{0.2}Hf_{0.2}Ti_{0.2}Nb_{0.2}Ta_{0.2})C$. *J. Mater. Sci. Technol.* **35**, 1700–1705 (2019).
33. Tsai, D.-C. et al. Oxidation resistance and characterization of (AlCrMoTaTi)–Si_x–N coating deposited via magnetron sputtering. *J. Alloys Compd.* **647**, 179–188 (2015).
34. Vladescu, A. et al. *In vitro* biocompatibility of Si alloyed multi-principal element carbide coatings. *PLOS ONE* **11**, e0161151 (2016).
35. Zhou, J. et al. High-entropy carbide: a novel class of multicomponent ceramics. *Ceram. Int.* **44**, 22014–22018 (2018).
36. Sarkar, A. et al. High entropy oxides for reversible energy storage. *Nat. Commun.* **9**, 3400 (2018).
37. Zheng, Y. et al. A high-entropy metal oxide as chemical anchor of polysulfide for lithium-sulfur batteries. *Energy Storage Mater.* **23**, 678–683 (2019).
38. Wang, Q. et al. Multi-anionic and -cationic compounds: new high entropy materials for advanced Li-ion batteries. *Energy Environ. Sci.* **12**, 2433–2442 (2019).
39. Cheng, K.-H., Tsai, C.-W., Lin, S.-J. & Yeh, J.-W. Effects of silicon content on the structure and mechanical properties of (AlCrTaTiZr)–Si_x–N coatings by reactive RF magnetron sputtering. *J. Phys. D* **44**, 205405 (2011).
40. Hsieh, M.-H., Tsai, M.-H., Shen, W.-J. & Yeh, J.-W. Structure and properties of two Al–Cr–Nb–Si–Ti high-entropy nitride coatings. *Surf. Coat. Technol.* **221**, 118–123 (2013).
41. Braun, J. L. et al. Charge-induced disorder controls the thermal conductivity of entropy-stabilized oxides. *Adv. Mater.* **30**, 1805004 (2018).
42. Lai, C.-H., Lin, S.-J., Yeh, J.-W. & Chang, S.-Y. Preparation and characterization of AlCrTaTiZr multi-element nitride coatings. *Surf. Coat. Technol.* **201**, 3275–3280 (2006).
43. Huang, P.-K. & Yeh, J.-W. Effects of substrate bias on structure and mechanical properties of (AlCrNbSiTiV)N coatings. *J. Phys. D* **42**, 115401 (2009).
44. Huang, P.-K. & Yeh, J.-W. Inhibition of grain coarsening up to 1000 °C in (AlCrNbSiTiV)N superhard coatings. *Scr. Mater.* **62**, 105–108 (2010).
45. Harrington, T. J. et al. Phase stability and mechanical properties of novel high entropy transition metal carbides. *Acta Mater.* **166**, 271–280 (2019).
46. Stevanović, V., Lany, S., Zhang, X. & Zunger, A. Correcting density functional theory for accurate predictions of compound enthalpies of formation: fitted elemental-phase reference energies. *Phys. Rev. B* **85**, 115104 (2012).
47. Friedrich, R. et al. Coordination corrected ab initio formation enthalpies. *npj Comput. Mater.* **5**, 59 (2019).
48. Toher, C., Oses, C., Hicks, D. & Curtarolo, S. Unavoidable disorder and entropy in multi-component systems. *npj Comput. Mater.* **5**, 69 (2019).
49. van de Walle, A. Multicomponent multisublattice alloys, nonconfigurational entropy and other additions to the alloy theoretic automated toolkit. *Calphad* **33**, 266–278 (2009).
50. Lederer, Y., Toher, C., Vecchio, K. S. & Curtarolo, S. The search for high entropy alloys: a high-throughput *ab-initio* approach. *Acta Mater.* **159**, 364–383 (2018).
51. Chen, T.-K., Shun, T. T., Yeh, J.-W. & Wong, M. S. Nanostructured nitride films of multi-element high-entropy alloys by reactive DC sputtering. *Surf. Coat. Technol.* **188–189**, 193–200 (2004).
52. Chen, T.-K., Wong, M.-S., Shun, T.-T. & Yeh, J.-W. Nanostructured nitride films of multi-element high-entropy alloys by reactive DC sputtering. *Surf. Coat. Technol.* **200**, 1361–1365 (2005).
53. Huang, Y.-S., Chen, L., Lui, H.-W., Cai, M.-H. & Yeh, J.-W. Microstructure, hardness, resistivity and thermal stability of sputtered oxide films of $AlCoCrCu_{0.5}NiFe$ high-entropy alloy. *Mater. Sci. Eng. A* **457**, 77–83 (2007).
54. Chen, T.-K. & Wong, M.-S. Structure and properties of reactively-sputtered $Al_xCoCrCuFeNi$ oxide films. *Thin Solid. Films* **516**, 141–146 (2007).
55. Anand, G., Wynn, A. P., Handley, C. M. & Freeman, C. L. Phase stability and distortion in high-entropy oxides. *Acta Mater.* **146**, 119–125 (2018).
56. Yang, Y., Wang, W., Gan, G.-Y., Shi, X.-F. & Tang, B.-Y. Structural, mechanical and electronic properties of (TaNbHfTiZr)C high entropy carbide under pressure: ab initio investigation. *Phys. B* **550**, 163–170 (2018).
57. Zunger, A., Wei, S.-H., Ferreira, L. G. & Bernard, J. E. Special quasirandom structures. *Phys. Rev. Lett.* **65**, 353–356 (1990).
58. Ye, B. et al. First-principles study, fabrication and characterization of $(Zr_{0.25}Nb_{0.25}Ti_{0.25}V_{0.25})C$ high-entropy ceramics. *Acta Mater.* **170**, 15–23 (2019).
59. Yang, K., Oses, C. & Curtarolo, S. Modeling off-stoichiometry materials with a high-throughput *ab-initio* approach. *Chem. Mater.* **28**, 6484–6492 (2016).
60. Rák, Zs. et al. Charge compensation and electrostatic transferability in three entropy-stabilized oxides: results from density functional theory calculations. *J. Appl. Phys.* **120**, 095105 (2016).
61. Rost, C. M., Rák, Zs., Brenner, D. W. & Maria, J.-P. Local structure of the $Mg_xNi_xCo_xCu_xZn_xO$(x = 0.2) entropy-stabilized oxide: an EXAFS study. *J. Amer. Ceram. Soc.* **100**, 2732–2738 (2017).
62. Rák, Zs., Maria, J.-P. & Brenner, D. W. Evidence for Jahn–Teller compression in the (Mg, Co, Ni, Cu, Zn)O entropy-stabilized oxide: a DFT study. *Mater. Lett.* **217**, 300–303 (2018).
63. Bērardan, D., Franger, S., Dragoe, D., Meena, A. K. & Dragoe, N. Colossal dielectric constant in high entropy oxides. *Phys. Stat. Solidi Rapid Res. Lett.* **10**, 328–333 (2016).
64. Bērardan, D., Franger, S., Meena, A. K. & Dragoe, N. Room temperature lithium superionic conductivity in high entropy oxides. *J. Mater. Chem. A* **4**, 9536–9541 (2016).
65. Osenciat, N. et al. Charge compensation mechanisms in Li-substituted high-entropy oxides and influence on Li superionic conductivity. *J. Amer. Ceram. Soc.* **102**, 6156–6162 (2019).
66. Bērardan, D., Meena, A. K., Franger, S., Herrero, C. & Dragoe, N. Controlled Jahn–Teller distortion in (MgCoNiCuZn)O-based high entropy oxides. *J. Alloys Compd.* **704**, 693–700 (2017).
67. Kaufman, L. & Bernstein, H. *Computer Calculation of Phase Diagrams with Special Reference to Refractory Metals* (Academic Press, 1970).
68. Saunders, N. & Miodownik, A. P. *CALPHAD (Calculation of Phase Diagrams): A Comprehensive Guide* (Elsevier Science, 1998).
69. Zhong, Y. et al. Exploration of high entropy ceramics (HECs) with computational thermodynamics — a case study with $LaMnO_{3\pm\delta}$. *Mater. Des.* **182**, 108060 (2019).
70. Wang, Y.-P., Gan, G.-Y., Wang, W., Yang, Y. & Tang, B.-Y. Ab initio prediction of mechanical and electronic properties of ultrahigh temperature high-entropy ceramics $(Hf_{0.2}Zr_{0.2}Ta_{0.2}M_{0.2}Ti_{0.2})B_2$ (M = Nb, Mo, Cr). *Phys. Stat. Solidi B* **255**, 1800011 (2018).
71. Zhang, Q., Zhang, J., Li, N. & Chen, W. Understanding the electronic structure, mechanical properties, and thermodynamic stability of (TiZrHfNbTa)C combined experiments and first-principles simulation. *J. Appl. Phys.* **126**, 025101 (2019).
72. Dupuy, A. D., Wang, X. & Schoenung, J. M. Entropic phase transformation in nanocrystalline high entropy oxides. *Mater. Res. Lett.* **7**, 60–67 (2019).
73. Sarkar, A. et al. Nanocrystalline multicomponent entropy stabilised transition metal oxides. *J. Eur. Ceram. Soc.* **37**, 747–754 (2017).
74. Chen, H. et al. Entropy-stabilized metal oxide solid solutions as CO oxidation catalysts with high-temperature stability. *J. Mater. Chem. A* **6**, 11129–11133 (2018).
75. Biesuz, M., Spiridigliozzi, L., Dell'Agli, G., Bortolotti, M. & Sglavo, V. M. Synthesis and sintering of (Mg, Co, Ni, Cu, Zn)O entropy-stabilized oxides obtained by wet chemical methods. *J. Mater. Sci.* **53**, 8074–8085 (2018).
76. Mao, A. et al. Solution combustion synthesis and magnetic property of rock-salt $(Co_{0.2}Cu_{0.2}Mg_{0.2}Ni_{0.2}Zn_{0.2})O$ high-entropy oxide nanocrystalline powder. *J. Magn. Magn. Mater.* **484**, 245–252 (2019).
77. Chen, H. et al. Mechanochemical synthesis of high entropy oxide materials under ambient conditions: dispersion of catalysts via entropy maximization. *ACS Mater. Lett.* **1**, 83–88 (2019).
78. Balcerzak, M., Kawamura, K., Bobrowski, R., Rutkowski, P. & Brylewski, T. Mechanochemical synthesis of (Co,Cu,Mg,Ni,Zn)O high-entropy oxide and its physicochemical properties. *J. Elec. Mater.* **48**, 7105–7113 (2019).
79. Kotsonis, G. N., Rost, C. M., Harris, D. T. & Maria, J.-P. Epitaxial entropy-stabilized oxides: growth of chemically diverse phases via kinetic bombardment. *MRS Commun.* **8**, 1371–1377 (2018).
80. Manthiram, A., Yu, X. & Wang, S. Lithium battery chemistries enabled by solid-state electrolytes. *Nat. Rev. Mater.* **2**, 16103 (2017).
81. Meisenheimer, P. B. et al. Magnetic frustration control through tunable stereochemically driven disorder in entropy-stabilized oxides. *Phys. Rev. Mater.* **3**, 104420 (2019).
82. Hong, W. et al. Microstructural evolution and mechanical properties of (Mg,Co,Ni,Cu,Zn)O high-entropy ceramics. *J. Amer. Ceram. Soc.* **102**, 2228–2237 (2019).
83. Diercks, D. R., Brennecka, G., Gorman, B. P., Rost, C. M. & Maria, J.-P. Nanoscale compositional analysis of a thermally processed entropy-stabilized oxide via correlative TEM and APT. *Microsc. Microanal.* **23**, 1640–1641 (2017).
84. Meisenheimer, P. B., Kratofil, T. J. & Heron, J. T. Giant enhancement of exchange coupling in entropy-stabilized oxide heterostructures. *Sci. Rep.* **7**, 13344 (2017).
85. Jimenez-Segura, M. P. et al. Long-range magnetic ordering in rocksalt-type high-entropy oxides. *Appl. Phys. Lett.* **114**, 122401 (2019).
86. Zhang, J. et al. Long-range antiferromagnetic order in a rocksalt high entropy oxide. *Chem. Mater.* **31**, 3705–3711 (2019).
87. Djenadic, R. et al. Multicomponent equiatomic rare earth oxides. *Mater. Res. Lett.* **5**, 102–109 (2017).
88. Sarkar, A. et al. Multicomponent equiatomic rare earth oxides with a narrow band gap and associated praseodymium multivalency. *Dalton Trans.* **46**, 12167–12176 (2017).
89. Gild, J. et al. High-entropy fluorite oxides. *J. Eur. Ceram. Soc.* **38**, 3578–3584 (2018).
90. Chen, K. et al. A five-component entropy-stabilized fluorite oxide. *J. Eur. Ceram. Soc.* **38**, 4161–4164 (2018).
91. Jiang, S. et al. A new class of high-entropy perovskite oxides. *Scr. Mater.* **142**, 116–120 (2018).
92. Biesuz, M. et al. High entropy $Sr((Zr_{0.94}Y_{0.06})_{0.2}Sn_{0.2}Ti_{0.2}Hf_{0.2}Mn_{0.2})O_{3-x}$ perovskite synthesis by reactive spark plasma sintering. *J. Asian Ceram. Soc.* **7**, 127–132 (2019).
93. Oses, C., Toher, C. & Curtarolo, S. Data-driven design of inorganic materials with the Automatic Flow Framework for Materials Discovery. *MRS Bull.* **43**, 670–675 (2018).
94. Mehl, M. J. et al. The AFLOW library of crystallographic prototypes: part 1. *Comput. Mater. Sci.* **136**, S1–S828 (2017).
95. Hicks, D. et al. The AFLOW library of crystallographic prototypes: part 2. *Comput. Mater. Sci.* **161**, S1–S1011 (2019).
96. Witte, R. et al. High-entropy oxides: an emerging prospect for magnetic rare-earth transition metal perovskites. *Phys. Rev. Mater.* **3**, 034406 (2019).
97. Dąbrowa, J. et al. Synthesis and microstructure of the $(Co,Cr,Fe,Mn,Ni)_3O_4$ high entropy oxide characterized by spinel structure. *Mater. Lett.* **216**, 32–36 (2018).
98. Mao, A. et al. Facile synthesis and ferrimagnetic property of spinel $(CoCrFeMnNi)_3O_4$ high-entropy

oxide nanocrystalline powder. *J. Mol. Struct.* **1194**, 11–18 (2019).
99. Mao, A. et al. A new class of spinel high-entropy oxides with controllable magnetic properties. *J. Magn. Magn. Mater.* **497**, 165884 (2020).
100. Vinnik, D. A. et al. High-entropy oxide phases with magnetoplumbite structure. *Ceram. Int.* **45**, 12942–12948 (2019).
101. Vinnik, D. A. et al. Extremely polysubstituted magnetic material based on magnetoplumbite with a hexagonal structure: synthesis, structure, properties, prospects. *Nanomater.* **9**, 559 (2019).
102. Tseng, K.-P., Yang, Q., McCormack, S. J. & Kriven, W. M. High-entropy, phase-constrained, lanthanide sesquioxide. *J. Amer. Ceram. Soc.* **103**, 569–576 (2019).
103. Chen, H., Xiang, H., Dai, F.-Z., Liu, J. & Zhou, Y. High entropy $(Yb_{0.25}Y_{0.25}Lu_{0.25}Er_{0.25})_2SiO_5$ with strong anisotropy in thermal expansion. *J. Mater. Sci. Technol.* **36**, 134–139 (2020).
104. Zhao, Z., Xiang, H., Dai, F.-Z., Peng, Z. & Zhou, Y. $(La_{0.2}Ce_{0.2}Nd_{0.2}Sm_{0.2}Eu_{0.2})_2Zr_2O_7$: a novel high-entropy ceramic with low thermal conductivity and sluggish grain growth rate. *J. Mater. Sci. Technol.* **35**, 2647–2651 (2019).
105. Li, F., Zhou, L., Liu, J.-X., Liang, Y. & Zhang, G.-J. High-entropy pyrochlores with low thermal conductivity for thermal barrier coating materials. *J. Adv. Ceram.* **8**, 576–582 (2019).
106. Zhang, J. et al. High-entropy oxides $10La_2O_3$–$20TiO_2$–$10Nb_2O_5$–$20WO_3$–$20ZrO_2$ amorphous spheres prepared by containerless solidification. *Mater. Lett.* **244**, 167–170 (2019).
107. Feng, L., Fahrenholtz, W. G., Hilmas, G. E. & Zhou, Y. Synthesis of single-phase high-entropy carbide powders. *Scr. Mater.* **162**, 90–93 (2019).
108. Ye, B., Ning, S., Liu, D., Wen, T. & Chu, Y. One-step synthesis of coral-like high-entropy metal carbide powders. *J. Amer. Ceram. Soc.* **102**, 6372–6378 (2019).
109. Feng, L., Fahrenholtz, W. G. & Hilmas, G. E. Low-temperature sintering of single-phase, high-entropy carbide ceramics. *J. Amer. Ceram. Soc.* **102**, 7217–7224 (2019).
110. Wei, X.-F. et al. High entropy carbide ceramics from different starting materials. *J. Eur. Ceram. Soc.* **39**, 2989–2994 (2019).
111. Liu, D., Wen, T., Ye, B. & Chu, Y. Synthesis of superfine high-entropy metal diboride powders. *Scr. Mater.* **167**, 110–114 (2019).
112. Zhang, Y. et al. Dense high-entropy boride ceramics with ultra-high hardness. *Scr. Mater.* **164**, 135–139 (2019).
113. Zhang, Y. et al. Microstructure and mechanical properties of high-entropy borides derived from boro/carbothermal reduction. *J. Eur. Ceram. Soc.* **39**, 3920–3924 (2019).
114. Liu, D., Liu, H., Ning, S., Ye, B. & Chu, Y. Synthesis of high-purity high-entropy metal diboride powders by boro/carbothermal reduction. *J. Amer. Ceram. Soc.* **102**, 7071–7076 (2019).
115. Chicardi, E., García-Garrido, C. & Gotor, F. J. Low temperature synthesis of an equiatomic $(TiZrHfVNb)C_5$ high entropy carbide by a mechanically-induced carbon diffusion route. *Ceram. Int.* **45**, 21858–21863 (2019).
116. Qiu, N. et al. A high entropy oxide $(Mg_{0.2}Co_{0.2}Ni_{0.2}Cu_{0.2}Zn_{0.2}O)$ with superior lithium storage performance. *J. Alloys Compd.* **777**, 767–774 (2019).
117. Wang, Q. et al. High entropy oxides as anode material for Li-ion battery applications: a practical approach. *Electrochem. Commun.* **100**, 121–125 (2019).
118. Lu, X. et al. Improving the cycling stability of metal–nitride supercapacitor electrodes with a thin carbon shell. *Adv. Energy Mater.* **4**, 1300994 (2014).
119. Zhai, S. et al. The use of poly-cation oxides to lower the temperature of two-step thermochemical water splitting. *Energy Environ. Sci.* **11**, 2172–2178 (2018).
120. Zhang, G. et al. High entropy alloy as a highly active and stable electrocatalyst for hydrogen evolution reaction. *Electrochim. Acta* **279**, 19–23 (2018).
121. Wang, A.-L., Wan, H.-C., Xu, H., Tong, Y.-X. & Li, G.-R. Quinary PdNiCoCuFe alloy nanotube arrays as efficient electrocatalysts for methanol oxidation. *Electrochim. Acta* **127**, 448–453 (2014).
122. Löffler, T. et al. Discovery of a multinary noble metal-free oxygen reduction catalyst. *Adv. Energy Mater.* **8**, 1802269 (2018).
123. Batchelor, T. A. A. et al. High-entropy alloys as a discovery platform for electrocatalysis. *Joule* **3**, 834–845 (2019).
124. Cui, X., Zhang, B., Zeng, C. & Guo, S. Electrocatalytic activity of high-entropy alloys toward oxygen evolution reaction. *MRS Commun.* **8**, 1230–1235 (2018).
125. Xie, P. et al. Highly efficient decomposition of ammonia using high-entropy alloy catalysts. *Nat. Commun.* **10**, 4011 (2019).
126. Yusenko, K. V. et al. First hexagonal close packed high-entropy alloy with outstanding stability under extreme conditions and electrocatalytic activity for methanol oxidation. *Scr. Mater.* **138**, 22–27 (2017).
127. Qiu, H.-J. et al. Nanoporous high-entropy alloys for highly stable and efficient catalysts. *J. Mater. Chem. A* **7**, 6499–6506 (2019).
128. Yao, Y. et al. Carbothermal shock synthesis of high-entropy-alloy nanoparticles. *Science* **359**, 1489–1494 (2018).
129. Lv, Z. Y. et al. Development of a novel high-entropy alloy with eminent efficiency of degrading azo dye solutions. *Sci. Rep.* **6**, 34213 (2016).
130. Zhang, Z. et al. Mechanochemical nonhydrolytic sol–gel-strategy for the production of mesoporous multimetallic oxides. *Chem. Mater.* **31**, 5529–5536 (2019).
131. Gong, K., Du, F., Xia, Z., Durstock, M. & Dai, L. Nitrogen-doped carbon nanotube arrays with high electrocatalytic activity for oxygen reduction. *Science* **323**, 760–764 (2009).
132. Lefèvre, M., Proietti, E., Jaouen, F. & Dodelet, J.-P. Iron-based catalysts with improved oxygen reduction activity in polymer electrolyte fuel cells. *Science* **324**, 71–74 (2009).
133. Jaouen, F. et al. Recent advances in non-precious metal catalysis for oxygen-reduction reaction in polymer electrolyte fuel cells. *Energy Environ. Sci.* **4**, 114–130 (2011).
134. Li, Y. et al. An oxygen reduction electrocatalyst based on carbon nanotube–graphene complexes. *Nat. Nanotechnol.* **7**, 394–400 (2012).
135. Banham, D. et al. A review of the stability and durability of non-precious metal catalysts for the oxygen reduction reaction in proton exchange membrane fuel cells. *J. Power Sources* **285**, 334–348 (2015).
136. Lu, Z. et al. High-efficiency oxygen reduction to hydrogen peroxide catalysed by oxidized carbon materials. *Nat. Catal.* **1**, 156–162 (2018).
137. Venkadesan, G. & Muthusamy, J. Experimental investigation of Al_2O_3/8YSZ and CeO_2/8YSZ plasma sprayed thermal barrier coating on diesel engine. *Ceram. Int.* **45**, 3166–3176 (2019).
138. Roychowdhury, S., Ghosh, T., Arora, R., Waghmare, U. V. & Biswas, K. Stabilizing *n*-type cubic GeSe by entropy-driven alloying of $AgBiSe_2$: ultralow thermal conductivity and promising thermoelectric performance. *Angew. Chem. Int. Ed.* **57**, 15167–15171 (2018).
139. Yang, Y.-C., Tsau, C.-H. & Yeh, J.-W. TiFeCoNi oxide thin film — a new composition with extremely low electrical resistivity at room temperature. *Scr. Mater.* **64**, 173–176 (2011).
140. Tsau, C.-H., Yang, Y.-C., Lee, C.-C., Wu, L.-Y. & Huang, H.-J. The low electrical resistivity of the high-entropy alloy oxide thin films. *Procedia Eng.* **36**, 246–252 (2012).
141. Dedoncker, R., Radnóczi, G., Abadias, G. & Depla, D. Reactive sputter deposition of CoCrCuFeNi in oxygen/argon mixtures. *Surf. Coat. Technol.* **378**, 124362 (2019).
142. Braic, V., Vladescu, A., Balaceanu, M., Luculescu, C. R. & Braic, M. Nanostructured multi-element (TiZrNbHfTa) N and (TiZrNbHfTa)C hard coatings. *Surf. Coat. Technol.* **211**, 117–121 (2012).
143. Lin, M.-I., Tsai, M.-H., Shen, W.-J. & Yeh, J.-W. Evolution of structure and properties of multi-component $(AlCrTaTiZr)O_x$ films. *Thin Solid Films* **518**, 2732–2737 (2010).
144. Tsai, M.-H., Wang, C.-W., Lai, C.-H., Yeh, J.-W. & Gan, J.-Y. Thermally stable amorphous $(AlMoNbSiTaTiVZr)_{50}N_{50}$ nitride film as diffusion barrier in copper metallization. *Appl. Phys. Lett.* **92**, 052109 (2008).
145. Chang, S.-Y., Li, C.-E., Chiang, S.-C. & Huang, Y.-C. 4-nm thick multilayer structure of multi-component $(AlCrRuTaTiZr)N_x$ as robust diffusion barrier for Cu interconnects. *J. Alloys Compd.* **515**, 4–7 (2012).
146. Chang, S.-Y., Chen, M.-K. & Chen, D.-S. Multiprincipal-element AlCrTaTiZr–nitride nanocomposite film of extremely high thermal stability as diffusion barrier for Cu metallization. *J. Electrochem. Soc.* **156**, G37–G42 (2009).
147. Chang, S.-Y. et al. Improved diffusion-resistant ability of multicomponent nitrides: from unitary TiN to senary high-entropy (TiTaCrZrAlRu)N. *JOM* **65**, 1790–1796 (2013).
148. Sharma, Y. et al. Single-crystal high entropy perovskite oxide epitaxial films. *Phys. Rev. Mater.* **2**, 060404 (2018).
149. Braic, V. et al. Characterization of multi-principal-element (TiZrNbHfTa)N and (TiZrNbHfTa)C coatings for biomedical applications. *J. Mech. Behav. Biomed. Mater.* **10**, 197–205 (2012).
150. Wang, Y., Jie, W., Yang, C., Wei, X. & Hao, J. Colossal permittivity materials as superior dielectrics for diverse applications. *Adv. Func. Mater.* **29**, 1808118 (2019).
151. Leyland, A. & Matthews, A. On the significance of the *H/E* ratio in wear control: a nanocomposite coating approach to optimised tribological behaviour. *Wear* **246**, 1–11 (2000).
152. Li, Z., Pradeep, K. G., Deng, Y., Raabe, D. & Tasan, C. C. Metastable high-entropy dual-phase alloys overcome the strength–ductility trade-off. *Nature* **534**, 227–230 (2016).
153. Troparevsky, M. C., Morris, J. R., Kent, P. R. C., Lupini, A. R. & Stocks, G. M. Criteria for predicting the formation of single-phase high-entropy alloys. *Phys. Rev. X* **5**, 011041 (2015).
154. Widom, M. in *High-Entropy Alloys: Fundamentals and Applications* Ch. 8 (eds Gao, M. C., Yeh, J.-W., Liaw, P. K. & Zhang, Y.) 267–298 (Springer, 2016).
155. Huhn, W. P. & Widom, M. Prediction of A2 to B2 phase transition in the high entropy alloy Mo–Nb–Ta–W. *JOM* **65**, 1772–1779 (2013).
156. Widom, M. Entropy and diffuse scattering: comparison of NbTiVZr and CrMoNbV. *Metall. Mater. Trans. A* **47**, 3306–3311 (2016).
157. de Fontaine, D. in *Solid State Physics* Vol. 47 Ch. 2 (eds Ehrenreich, H. & Turnbull, D.) 33–176 (Academic Press, 1994).
158. van de Walle, A. & Asta, M. Self-driven lattice-model Monte Carlo simulations of alloy thermodynamic properties and phase diagrams. *Model. Simul. Mater. Sci. Eng.* **10**, 521 (2002).
159. Balluffi, R. W., Allen, S. M. & Carter, W. C. *Kinetics of Materials* (Wiley, 2005).
160. Ye, B., Wen, T., Huang, K., Wang, C.-Z. & Chu, Y. First-principles study, fabrication, and characterization of $(Hf_{0.2}Zr_{0.2}Ta_{0.2}Nb_{0.2}Ti_{0.2})C$ high-entropy ceramic. *J. Amer. Ceram. Soc.* **102**, 4344–4352 (2019).
161. Demirskyi, D. et al. High-temperature flexural strength performance of ternary high-entropy carbide consolidated via spark plasma sintering of TaC, ZrC and NbC. *Scr. Mater.* **164**, 12–16 (2019).
162. Peng, C. et al. Diffusion-controlled alloying of single-phase multi-principal transition metal carbides with high toughness and low thermal diffusivity. *Appl. Phys. Lett.* **114**, 011905 (2019).
163. Zhang, H. & Akhtar, F. Processing and characterization of refractory quaternary and quinary high-entropy carbide composite. *Entropy* **21**, 474 (2019).
164. Zhang, H., Hedman, D., Feng, P., Han, G. & Akhtar, F. A high-entropy $B_4(HfMo_2TaTi)C$ and SiC ceramic composite. *Dalton Trans.* **48**, 5161–5167 (2019).
165. Lai, C.-H., Cheng, K.-H., Lin, S.-J. & Yeh, J.-W. Mechanical and tribological properties of multi-element (AlCrTaTiZr)N coatings. *Surf. Coat. Technol.* **202**, 3732–3738 (2008).
166. Lin, C. H., Duh, J. G. & Yeh, J.-W. Multi-component nitride coatings derived from Ti–Al–Cr–Si–V target in RF magnetron sputter. *Surf. Coat. Technol.* **201**, 6304–6308 (2007).
167. Lin, C. H. & Duh, J. G. Corrosion behavior of $(Ti–Al–Cr–Si–V)_xN_y$ coatings on mild steels derived from RF magnetron sputtering. *Surf. Coat. Technol.* **203**, 558–561 (2008).
168. Chang, H.-W. et al. Influence of substrate bias, deposition temperature and post-deposition annealing on the structure and properties of multi-principal-component (AlCrMoSiTi)N coatings. *Surf. Coat. Technol.* **202**, 3360–3366 (2008).
169. Huang, P.-K. & Yeh, J.-W. Effects of nitrogen content on structure and mechanical properties of multi-element (AlCrNbSiTiV)N coating. *Surf. Coat. Technol.* **203**, 1891–1896 (2009).
170. Hsieh, T. H., Hsu, C. H., Wu, C. Y., Kao, J. Y. & Hsu, C. Y. Effects of deposition parameters on the structure and mechanical properties of high-entropy alloy nitride films. *Curr. Appl. Phys.* **18**, 512–518 (2018).
171. Liang, S.-C. et al. Effects of substrate temperature on the structure and mechanical properties of (TiVCrZrHf)N coatings. *Appl. Surf. Sci.* **257**, 7709–7713 (2011).
172. Cheng, K.-H., Lai, C.-H., Lin, S.-J. & Yeh, J.-W. Structural and mechanical properties of multi-element $(AlCrMoTaTiZr)N_x$ coatings by reactive magnetron sputtering. *Thin Solid. Films* **519**, 3185–3190 (2011).

173. Chang, S.-Y., Lin, S.-Y. & Huang, Y.-C. Microstructures and mechanical properties of multi-component (AlCrTaTiZr)N_xC_y nanocomposite coatings. *Thin Solid. Films* **519**, 4865–4869 (2011).
174. Lin, S.-Y., Chang, S.-Y., Huang, Y.-C., Shieu, F.-S. & Yeh, J.-W. Mechanical performance and nanoindenting deformation of (AlCrTaTiZr)NC_y multi-component coatings co-sputtered with bias. *Surf. Coat. Technol.* **206**, 5096–5102 (2012).
175. Lee, C.-T. et al. Effects of DC bias on the microstructure, residual stress and hardness properties of TiVCrZrTaN films by reactive RF magnetron sputtering. *Proc. Eng.* **36**, 316–321 (2012).
176. Chang, Z.-C., Tsai, D.-C. & Chen, E.-C. Structure and characteristics of reactive magnetron sputtered (CrTaTiVZr)N coatings. *Mater. Sci. Semiconductor Proc.* **39**, 30–39 (2015).
177. Hsueh, H.-T., Shen, W.-J., Tsai, M.-H. & Yeh, J.-W. Effect of nitrogen content and substrate bias on mechanical and corrosion properties of high-entropy films $(AlCrSiTiZr)_{100-x}N_x$. *Surf. Coat. Technol.* **206**, 4106–4112 (2012).
178. Sobol', O. V. et al. Reproducibility of the single-phase structural state of the multielement high-entropy Ti–V–Zr–Nb–Hf system and related superhard nitrides formed by the vacuum-arc method. *Tech. Phys. Lett.* **38**, 616–619 (2012).
179. Pogrebnjak, A. D. et al. Microstructure, physical and chemical properties of nanostructured (Ti–Hf–Zr–V–Nb)N coatings under different deposition conditions. *Mater. Chem. Phys.* **147**, 1079–1091 (2014).
180. Tsai, C.-W. et al. Strong amorphization of high-entropy AlBCrSiTi nitride film. *Thin Solid. Films* **520**, 2613–2618 (2012).
181. Braic, M., Balaceanu, M., Vladescu, A., Zoita, C. N. & Braic, V. Deposition and characterization of multi-principal-element (CuSiTiYZr)C coatings. *Appl. Surf. Sci.* **284**, 671–678 (2013).
182. Tsai, D.-C. et al. Structural morphology and characterization of (AlCrMoTaTi)N coating deposited via magnetron sputtering. *Appl. Surf. Sci.* **282**, 789–797 (2013).
183. Gorban', V. F. et al. Production and mechanical properties of high-entropic carbide based on the TiZrHfVNbTa multicomponent alloy. *J. Superhard Mater.* **39**, 166–171 (2017).
184. Malinovskis, P. et al. Synthesis and characterization of multicomponent (CrNbTaTiW)C films for increased hardness and corrosion resistance. *Mater. Des.* **149**, 51–62 (2018).
185. Jhong, Y.-S., Huang, C.-W. & Lin, S.-J. Effects of CH_4 flow ratio on the structure and properties of reactively sputtered (CrNbSiTiZr)C_x coatings. *Mater. Chem. Phys.* **210**, 348–352 (2018).
186. Mayrhofer, P. H., Kirnbauer, A., Ertelthaler, Ph. & Koller, C. M. High-entropy ceramic thin films; a case study on transition metal diborides. *Scr. Mater.* **149**, 93–97 (2018).
187. Chang, S.-Y. & Chen, D.-S. 10-nm-thick quinary (AlCrTaTiZr)N film as effective diffusion barrier for Cu interconnects at 900 °C. *Appl. Phys. Lett.* **94**, 231909 (2009).
188. Liang, S.-C. et al. Thermally stable TiVCrZrHf nitride films as diffusion barriers in copper metallization. *Electrochem. Solid-State Lett.* **15**, H5–H8 (2012).
189. Tsai, D.-C. et al. Interfacial reactions and characterization of (TiVCrZrHf)N thin films during thermal treatment. *Surf. Coat. Technol.* **240**, 160–166 (2014).
190. Tsau, C.-H., Hwang, Z.-Y. & Chen, S.-K. The microstructures and electrical resistivity of (Al, Cr, Ti) $FeCoNiO_x$ high-entropy alloy oxide thin films. *Adv. Mater. Sci. Eng.* **2015**, 353140 (2015).
191. Dinu, M. et al. In vitro corrosion resistance of Si containing multi-principal element carbide coatings. *Mater. Corros.* **67**, 908–914 (2016).
192. Sarkar, A. et al. High-entropy oxides: fundamental aspects and electrochemical properties. *Adv. Mater.* **31**, 1806236 (2019).
193. Chellali, M. R. et al. On the homogeneity of high entropy oxides: an investigation at the atomic scale. *Scr. Mater.* **166**, 58–63 (2019).
194. Urban, A., Abdellahi, A., Dacek, S., Artrith, N. & Ceder, G. Electronic-structure origin of cation disorder in transition-metal oxides. *Phys. Rev. Lett.* **119**, 176402 (2017).

Acknowledgements
The authors thank K. Vecchio, J.-P. Maria, E. Opila, P. Hopkins, J. Luo, D. Brenner, D. Hicks, Y. Lederer, O. Levy and X. Campilongo for fruitful discussions. Research sponsored by DOD-ONR (N00014-15-1-2863, N00014-16-1-2326, N00014-17-1-2876).

Author contributions
S.C., C.O. and C.T. performed the literature search. All authors contributed equally to the article.

Competing interests
The authors declare no competing interests.

Publisher's note
Springer Nature remains neutral with regard to jurisdictional claims in published maps and institutional affiliations.

RELATED LINKS
AB3C6_cI80_206_a_d_e (bixbyite structure): http://aflow.org/CrystalDatabase/AB3C6_cI80_206_a_d_e
AB3C_oP20_62_c_cd_a (orthorhombic perovskite structure): http://aflow.org/CrystalDatabase/AB3C_oP20_62_c_cd_a
A3B4_cF56_227_ad_e (spinel structure): http://aflow.org/CrystalDatabase/A3B4_cF56_227_ad_e
A2B2C7_cF88_227_c_d_af (pyrochlore structure): http://aflow.org/CrystalDatabase/A2B2C7_cF88_227_c_d_af
A7B2C2_mC22_12_aij_h_i (thortveitite structure): http://aflow.org/CrystalDatabase/A7B2C2_mC22_12_aij_h_i
AB_cF8_225_a_b (rock-salt structure): http://aflow.org/CrystalDatabase/AB_cF8_225_a_b
AB2_cF12_225_a_c (fluorite structure): http://aflow.org/CrystalDatabase/AB2_cF12_225_a_c
AB3C_cP5_221_a_c_b (cubic perovskite structure): http://aflow.org/CrystalDatabase/AB3C_cP5_221_a_c_b
AB2_hP3_191_a_d (AlB_2 structure): http://aflow.org/CrystalDatabase/AB2_hP3_191_a_d
AB2_hP9_180_d_j (C40 structure): http://aflow.org/CrystalDatabase/AB2_hP9_180_d_j